

On the Correlations between Galaxy Properties and Supermassive Black Hole Mass

A. Beifiori^{1,2*}, S. Courteau³, E. M. Corsini⁴, and Y. Zhu³

¹Max-Planck-Institut für Extraterrestrische Physik, Giessenbachstraße, D-85748 Garching, Germany

²Institute of Cosmology and Gravitation, Dennis Sciama Building, Burnaby Road, Portsmouth, PO1 3FX, United Kingdom

³Queen's University, Department of Physics, Engineering Physics and Astronomy, Kingston, ON, K7L 3N6, Canada

⁴Dipartimento di Astronomia, Università di Padova, vicolo dell'Osservatorio 3, I-35122 Padova, Italy

Accepted 2011 September 27. Received 2011 September 13; in original form 2011 January 5

ABSTRACT

We use a large sample of upper limits and accurate estimates of supermassive black holes (SMBHs) masses coupled with libraries of host galaxy velocity dispersions, rotational velocities and photometric parameters extracted from Sloan Digital Sky Survey *i*-band images to establish correlations between the SMBH and host galaxy parameters. We test whether the mass of the black hole, M_{\bullet} , is fundamentally driven by either local or global galaxy properties. We explore correlations between M_{\bullet} and stellar velocity dispersion σ_e , *i*-band bulge luminosity $L_{i,\text{bulge}}$, bulge mass M_{bulge} , bulge Sérsic index n , bulge mean effective surface brightness $\langle\mu_{e,\text{bulge}}\rangle$, *i*-band luminosity of the galaxy $L_{i,\text{gal}}$, galaxy stellar mass $M_{\star,\text{gal}}$, maximum circular velocity V_c , galaxy dynamical and effective masses $M_{\text{dyn,gal}}$ and $M_{e,\text{gal}}$. We verify the tightness of the $M_{\bullet} - \sigma_e$ relation and find that correlations with other galaxy parameters do not yield tighter trends. We do not find differences in the $M_{\bullet} - \sigma_e$ relation of barred and unbarred galaxies. The $M_{\bullet} - \sigma_e$ relation of pseudo-bulges is also coarser and has a different slope than that involving classical bulges. The $M_{\bullet} - M_{\text{bulge}}$ is not as tight as the $M_{\bullet} - \sigma_e$ relation, despite the bulge mass proving to be a better proxy of M_{\bullet} than bulge luminosity, and despite adding the bulge effective radius as an additional fitting parameter. Contrary to various published reports, we find a rather poor correlation between M_{\bullet} and n (or $\langle\mu_{e,\text{bulge}}\rangle$) suggesting that M_{\bullet} is not related to the bulge light concentration. The correlations between M_{\bullet} and galaxy luminosity or mass are not a marked improvement over the $M_{\bullet} - \sigma_e$ relation. These scaling relations depend sensitively on the host galaxy morphology: early-type galaxies follow a tighter relation than late-type galaxies. If V_c is a proxy for the dark matter halo mass, the large scatter of the $M_{\bullet} - V_c$ relation then suggests that M_{\bullet} is more coupled to the baryonic rather than the dark matter. We have tested the need for a third parameter in the M_{\bullet} scaling relations, through various linear correlations with bulge and galaxy parameters, only to confirm that the fundamental plane of the SMBH is mainly driven by σ_e with a small tilt due to the effective radius. We provide a compendium of galaxy structural properties for most of the SMBH hosts known to date.

Key words: black holes physics — galaxies: fundamental parameters — galaxies: photometry — galaxies: kinematics and dynamics — galaxies: statistics

1 INTRODUCTION

The mass M_{\bullet} of supermassive black holes (SMBHs) is closely tied to the properties of the spheroidal component of galaxies, such as the bulge luminosity, L_{bulge} (Dressler 1989; Kormendy & Richstone 1995; Marconi & Hunt

2003; Graham 2007; Gültekin et al. 2009, hereafter G09), the stellar velocity dispersion, σ (Ferrarese & Merritt 2000; Gebhardt et al. 2000; Tremaine et al. 2002; Ferrarese & Ford 2005; G09), the mass of the bulge (Magorrian et al. 1998; Häring & Rix 2004), the central light concentration (Graham et al. 2001), the Sérsic index (Graham & Driver 2007), the virial mass of the galaxy (Ferrarese et al. 2006), the gravitational binding energy

* E-mail: beifiori@mpe.mpg.de

(Aller & Richstone 2007), the kinetic energy of random motions of the bulge (Feoli & Mancini 2009), and the stellar light and mass deficit associated to the core ellipticals (Lauer et al. 2007; Kormendy & Bender 2009). Most of these relations are inter-compared in Novak et al. (2006) and in G09. Given the $M_{\bullet} - \sigma$ relation and the correlation between σ and the circular velocity, V_c , Ferrarese (2002) and Pizzella et al. (2005) suggested a link between M_{\bullet} and V_c (or equivalently, with the mass of the dark matter halo). However, Courteau et al. (2007) and Ho (2007) pointed out that the $V_c - \sigma$ relation actually depends on galaxy morphology (or equivalently, on its light concentration) thus precluding a simple connection between M_{\bullet} and V_c . Kormendy & Bender (2011) studied a sample of bulgeless galaxies and concluded that there is almost no correlation between the SMBH and dark matter halo, unless the galaxy also contains a bulge.

Several authors have noted that the residuals of the $M_{\bullet} - \sigma$ and $M_{\bullet} - L_{\text{bulge}}$ relations correlate with the galaxy effective radius (e.g., Marconi & Hunt 2003). Hopkins et al. (2007a,b) suggested the possibility of a linear combination between different galaxy properties to reduce the scatter of the M_{\bullet} scaling laws, heralding the idea of a fundamental plane of SMBHs (BHFP). Many SMBH scaling relations could thus be seen as projections of the BHFP (Aller & Richstone 2007; Barway & Kembhavi 2007). A correlation of M_{\bullet} with more than one galaxy parameter would suggest a SMBH growth sensitive to the overall structure of the host galaxy.

The local characterisation and cosmic evolution of the M_{\bullet} scaling relations have already been examined through theoretical models for the coevolution of galaxies and SMBHs (Granato et al. 2004; Vittorini et al. 2005; Hopkins et al. 2006; Monaco et al. 2007). These studies have revealed that the observed scaling relations could be reproduced in models of SMBH growth with strong feedback from the active galactic nucleus (AGN, Silk & Rees 1998; Cox et al. 2006; Robertson et al. 2006a,b; Di Matteo et al. 2005). In particular, these models predict the existence of the BHFP (Hopkins et al. 2007a,b, 2009). However, while the observed relations can be reproduced by the models, these still depend on the adopted slope, zero point, and scatter (Somerville 2009) which remain ill-constrained.

In this work, we make use of a large sample of galaxies with available M_{\bullet} estimates to improve our understanding of the known scaling laws over a wide range of M_{\bullet} , morphological type and nuclear activity, as well as to test for possible correlations of M_{\bullet} with different combinations of spheroid and galaxy parameters.

This paper is organised as follows. The sample of SMBH hosts is described in §2. Their photometric, kinematic, and dynamical properties are presented in §3, while the correlations between M_{\bullet} and the bulge and galaxy properties are shown in §4. We discuss our results and conclude in §5.

2 SAMPLE DESCRIPTION

The M_{\bullet} values were retrieved from two different samples: the compilation of M_{\bullet} upper limits by Beifiori et al. (2009, hereafter B09) and the compilation of secure M_{\bullet} by G09.

The M_{\bullet} estimates of B09 were obtained from *Hubble*

Space Telescope (HST) archival spectra. That sample includes nuclear spectra for 105 nearby galaxies with $D < 100$ Mpc obtained with the Space Telescope Imaging Spectrograph (STIS) equipped with the G750M grating. The spectra cover the region of the $H\alpha$ line and $[\text{N II}] \lambda\lambda 6548, 6583$ and $[\text{S II}] \lambda\lambda 6716, 6731$ doublets. The nebular-line widths were modelled in terms of gas motion in a thin disc of unknown orientation but known spatial extent following the method of Sarzi et al. (2002). B09 adopted two different inclinations for the gaseous disc with a nearly face-on disc ($i = 33^\circ$) hosting a larger M_{\bullet} and a nearly edge-on disc (81°) harbouring a smaller M_{\bullet} . The two inclinations correspond to the 68% upper and lower confidence limits for randomly oriented discs. We augmented the B09 sample with the M_{\bullet} upper limits of NGC 2892 and NGC 5921. The STIS/G750M spectra for these galaxies were retrieved from the HST archive and we have calculated their M_{\bullet} upper limits from the nebular line widths following the prescription of B09. We include in Sample A the set of 105 galaxies from B09 minus 18 galaxies in common with G09 (15 of them with a secure M_{\bullet} and 3 with a M_{\bullet} upper limit derived from the dynamical modelling of resolved kinematics). We are left with 87 M_{\bullet} upper limits from B09 based on nebular-line widths. We also include two newly determined M_{\bullet} upper limits and the five upper limits derived from the dynamical modelling of resolved kinematics by G09. The resulting 94 galaxies constitute our Sample A.

G09 collected M_{\bullet} data published up to November 2008 based on the resolved kinematics of ionised gas, stars, and water maser for total sample of 49 galaxies with a secure M_{\bullet} estimate and 18 galaxies with a M_{\bullet} upper limit. Our Sample B is limited to the 49 definite values of M_{\bullet} . The five upper limits derived from the dynamical modelling of resolved kinematics already belong to Sample A. The remaining 13 upper limits by G09 are taken from the nebular line width measurements by Sarzi et al. (2002). They were also measured by B09 and are therefore already included in Sample A.

All the data relative to Samples A and B are listed in Table 1 and 2, respectively. The upper limits by B09 were rescaled assuming $H_0 = 70 \text{ km s}^{-1} \text{ Mpc}^{-1}$, $\Omega_m = 0.3$, and $\Omega_\Lambda = 0.7$ to conform with G09.

Figure 1 shows the upper limits and the accurate determinations of M_{\bullet} for the 18 galaxies in common between the B09 and G09 samples. The M_{\bullet} estimates by B09 and G09 are consistent within 1σ of each other; no systematic offset is detected. Thus, nebular line width measurements by B09 (included in Sample A) trace well the nuclear gravitational potential dominated by the central SMBH, allowing a reliable estimate of M_{\bullet} (as those in Sample B). Therefore, we shall use the M_{\bullet} upper limits from Sample A to study the correlations of M_{\bullet} versus various galaxy parameters. We adopt for our tests the case of $i = 33^\circ$ which maximises the upper limit on M_{\bullet} . B09 already compared their $M_{\bullet} - \sigma_e$ relation with those of Ferrarese & Ford (2005) and Lauer et al. (2007) to show that their upper limits on M_{\bullet} (included in Sample A) are a valuable proxy for the more secure determinations of M_{\bullet} (comprised in Sample B). A Kolmogorov-Smirnov test on the distributions of M_{\bullet} and σ indicates that Samples A and B could be drawn from the same parent distribution to better than the 80% confidence level. For this reason, we merged Samples A and B into a

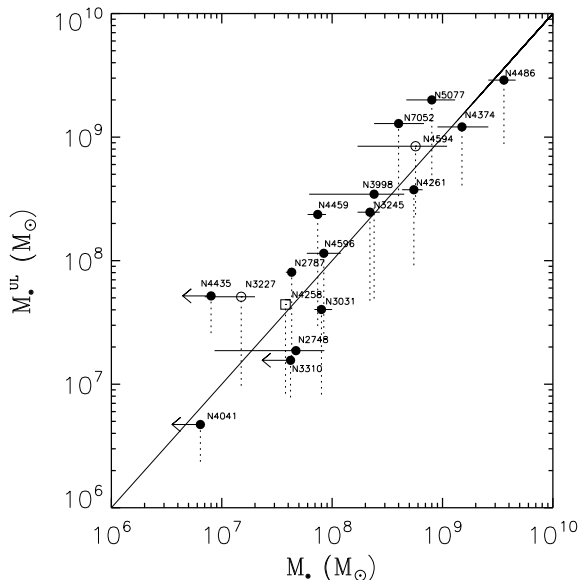


Figure 1. Comparison between the M_{\bullet} upper limits by B09 and accurate M_{\bullet} measurements (symbols) and upper limits (leftward arrows) by G09 and based on the resolved kinematics of gas (filled circles), stars (open circles), and water masers (open square). The upper and lower edges of the dotted lines correspond to B09’s M_{\bullet} values estimated assuming an inclination of $i = 33^{\circ}$ and 81° for the unresolved Keplerian disc, respectively.

joint A+B data set. The combination of Samples A and B yields a total sample of 143 M_{\bullet} determinations. The union of those two samples proves most valuable for the proper statistical assessment of scaling relations with M_{\bullet} .

3 GALAXY PROPERTIES

The aim of this study is to determine the strength of the correlations, if any, between M_{\bullet} and the properties of their host galaxies. For the latter, we have compiled as large a collection as possible of homogeneous measurements of photometric parameters (effective radius, effective surface brightness, Sérsic index, and luminosity of the bulge, effective radius, effective surface brightness, concentration, and total luminosity of the galaxy), kinematic properties (stellar velocity dispersion and circular velocity), and masses (bulge mass, galaxy stellar mass, virial and dynamical mass of the galaxy).

The sample demographics are as follows: 29% of the host galaxies are ellipticals, 27% lenticulars, and 44% are spirals (de Vaucouleurs et al. 1991, hereafter RC3). Regarding nuclear activity, 23% of the sample galaxies are Low-Ionisation Nuclear Emission-line Regions (LINERs), 11% host H II nuclei, 25% are Seyferts, and 8% are classified as transition objects according to Ho et al. (1997). The remaining 33% do not show central emission.

We describe in the sub-sections below the extraction of all the galaxy structural parameters.

3.1 Galaxy Photometric Parameters

We retrieved g and i -band images from the seventh data release (DR7, Abazajian et al. 2009) of the Sloan Digital Sky Survey (SDSS, York et al. 2000) for as many Sample A and B galaxies as possible. The total SDSS sample includes 90 galaxies, 62 from Sample A and 28 from Sample B, from which to derive structural parameters.

The SDSS images are already bias subtracted, flat-fielded and cleaned from bright stars; however, we performed our own sky subtraction since the SDSS pipeline sky levels may be flawed for extended galaxies (Bernardi et al. 2007; Lauer et al. 2007). This issue has been addressed in the SDSS-III Data Release 8 (Aihara et al. 2011; Blanton et al. 2011). For our purposes, we estimated the sky level of each galaxy image by isolating five regions away from the galaxy, free of any contaminant, and calculating the mode of the sky intensities per pixel within each sky region. The average and standard deviation of the five sky values was then computed. The difference between our measured sky values and those provided by SDSS can be as large as 4%. The SDSS sky level is always biased high, likely due to the inclusion of bright, extended sources while our interactive technique ensures a contaminant-free selection of the sky fields. We find that the typical surface brightness error in the g and i bands is $0.1 \text{ mag arcsec}^{-2}$ at $\mu_g \simeq 26 \text{ mag arcsec}^{-2}$ and $\mu_i \simeq 25 \text{ mag arcsec}^{-2}$, respectively (see McDonald et al. 2011, for more details). The large angular extent of NGC 224 and NGC 4594 relative to the field of view thwarted their proper sky subtraction; these two galaxies were therefore excluded from our SDSS sample. NGC 221 was also discarded due to improper positioning of the image on the detector. The remaining images were flux-calibrated based on the SDSS photometric zero-point, corrected for Galactic extinction (Schlegel et al. 1998) as well as for internal extinction and K -correction following Shao et al. (2007).

The galaxy surface brightness profiles were extracted using the isophotal fitting methods outlined in Courteau et al. (1996) and McDonald et al. (2011). These make use of the astronomical data reduction package XVISTA¹. The azimuthally-averaged surface brightness profiles, projected onto the major axis of each galaxy, are shown in Figure 2 for four sample galaxies. These are the elliptical galaxy NGC 5127, two high- (NGC 4036) and low- (NGC 4477) inclination lenticular galaxies, and the spiral galaxy NGC 3675 which boasts a remarkably high dust content.

The g and i -band total magnitude of each galaxy is then determined by summing the flux at each isophote and extrapolating the light profile to infinity. The $g - i$ colour of each galaxy was calculated from the difference of the fully corrected g and i -band magnitudes. The remaining structural parameters were measured from the i -band light profiles since, of all the SDSS band passes, the i -band suffers least dust extinction. We extracted the isophotal radius, $r_{24.5}$, corresponding to the surface brightness of $24.5 \text{ mag arcsec}^{-2}$, the half-light (or effective) radius of the galaxy, $r_{e,\text{gal}}$, the effective surface brightness of the galaxy, $\mu_{e,\text{gal}}$, and the galaxy concentration $C_{28} = 5 \log(r_{80}/r_{20})$, where r_{20} and r_{80} are the radii which enclose 20% and 80% of

¹ See <http://astronomy.nmsu.edu/holtz/xvista/index.html>.

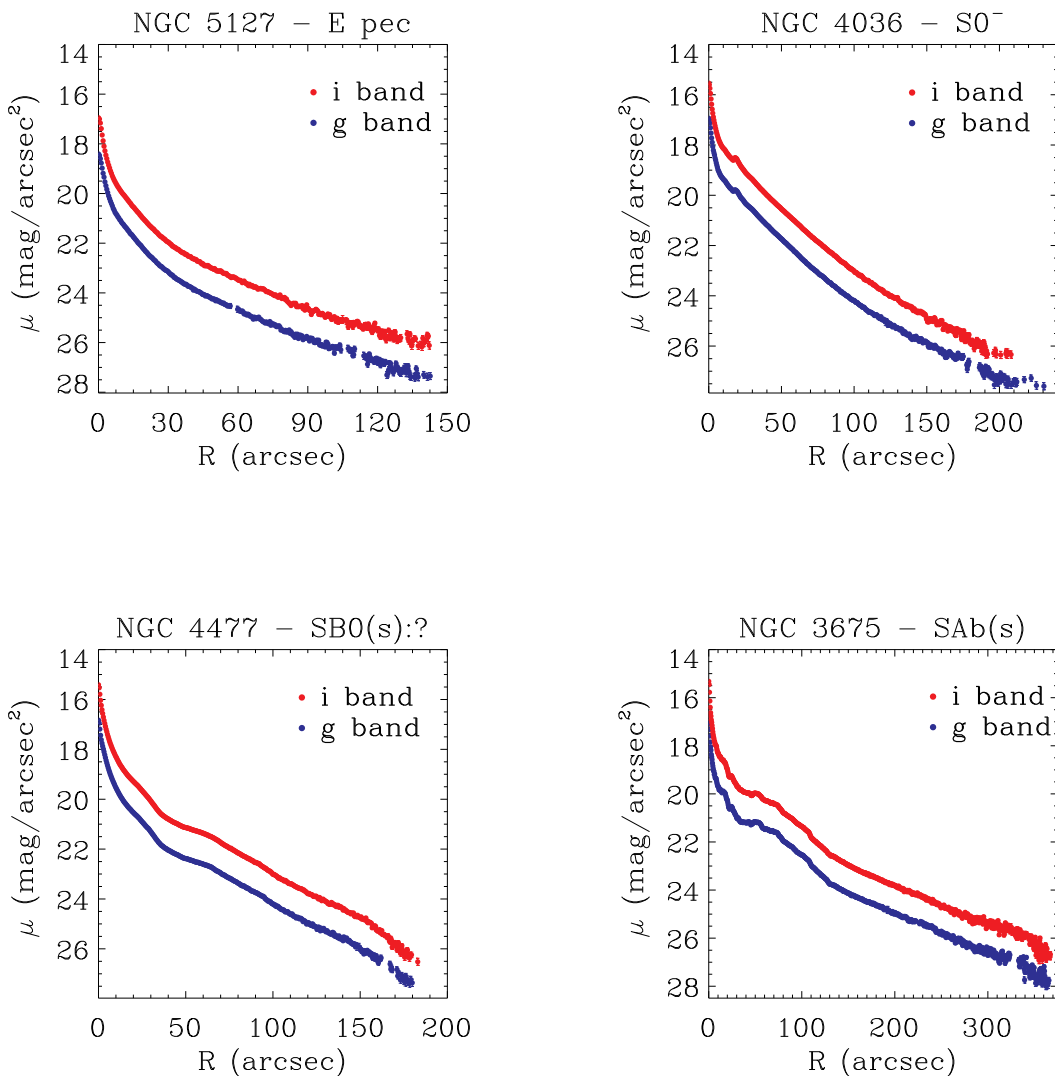


Figure 2. Typical g (red points) and i -band (blue points) surface brightness profiles extracted along the major axis for a few sample galaxies.

the total luminosity, respectively. These i -band structural parameters are listed in Table 3. The g -band magnitude is also listed. Based on simulated models of spiral galaxies (MacArthur et al. 2003), the typical error per galaxy structural parameter is roughly 10-20%.

3.2 Photometric Parameters of Bulges and Discs

The structural parameters for elliptical galaxies, modelled typically as a single spheroid, and for spiral galaxies, modelled as the sum of a spheroid and a disc, were derived by applying the two-dimensional photometric decomposition algorithm GASP2D (Méndez-Abreu et al. 2008) to the SDSS i -band images.

The surface brightness of the spheroid component (typ-

ically the entire elliptical galaxy or the bulge component for a disc galaxy) is modelled using a Sérsic function (Sérsic 1968; see also Graham & Driver 2005)

$$I_b(r) = I_e 10^{-b_n \left\{ \left(r/r_e \right)^{1/n} - 1 \right\}}, \quad (1)$$

where r_e is the effective radius, I_e is the surface brightness at r_e , and n is a shape parameter that describes the curvature of the radial profile. With $n = 1$ or $n = 4$, the Sérsic function reduces to the exponential or de Vaucouleurs function, respectively. The coefficient $b_n = 0.868 n - 0.142$ (Caon et al. 1993) is a normalisation term. The spheroid model elliptical isophotes have constant position angle PA_b and constant axial ratio q_b .

The surface brightness distribution of the disc component is assumed to follow an exponential law (Freeman 1970)

$$I_d(r) = I_0 e^{-r/h}, \quad (2)$$

where h and I_0 are the scale length and central surface brightness of the disc, respectively. The disc model elliptical isophotes have constant position angle PA_d and constant axial ratio q_d . The fitting algorithm GASP2D relies on a χ^2 minimisation of the intensities in counts, for which we must adopt initial trial parameters that are as close as possible to their final values. The latter were estimated from our ellipse-averaged light profiles from which basic fits to the bulge and disc were applied to estimate structural parameters (see Méndez-Abreu et al. 2008, for details). The χ^2 minimisation is based on the robust Levenberg-Marquardt method by Moré et al. (1980). The actual computation has been done using the MPFIT algorithm (Markwardt 2009) under the IDL² environment.

The GASP2D software yields structural parameters for the bulge (I_e , r_e , n , PA_b , and q_b) and disc (I_0 , h , PA_d , and q_d) and the position of the galaxy centre (x_0, y_0). In GASP2D, each image pixel intensity is weighted according to the variance of its total observed photon counts due to the contribution of both galaxy and sky, and accounting for photon and detector read-out noise. Seeing effects were taken into account by convolving the model image with a circular Moffat point spread function (Moffat 1969, hereafter PSF) with shape parameters measured from the stars in the galaxy image. Only the image pixels with an intensity larger than 1.5 times the sky standard deviation were included in the fit. Foreground stars were masked and excluded from the fit. The initial guesses were adopted to initialise the non-linear least-squares fit to galaxy image, where the parameters were all allowed to vary. A model of the galaxy surface brightness distribution was built using the fitted parameters. It was convolved with the adopted circular two-dimensional Moffat PSF and subtracted from the observed image to obtain a residual image. In order to confirm the minimum in the χ^2 -space found in this first pass, two more iterations were performed. In these iterations, all the pixels and/or regions of the residual image with values greater or less than a fixed threshold, controlled by the user, were rejected. Those regions were masked out and the fit was repeated assuming, as initial trials for the free parameters, the values obtained in the previous iteration. These masks are useful when galaxies have spiral arms and dust lanes, which can affect the fitted parameters. We found that our algorithm converges after three iterations.

The model decompositions for few elliptical galaxies (NGC 4473, NGC 4636, NGC 4649) were significantly improved by including a disc component, as found in a few other elliptical galaxies (Kormendy et al. 2009; McDonald et al. 2009). For the other ellipticals, the values of r_e obtained either directly (empirically) from the light profile (in §3.1) or by using a Sérsic fitting function (from the two-dimensional photometric decomposition) agree within their respective errors.

We eliminated 33 galaxies from our sample because of poor decompositions due to either a strong central bar, a Freeman II profile (Freeman 1970), or just the overall inadequacy of our single or double-component modelling (e.g.,

due to the presence of strong dust lanes and/or spiral arms). We successfully performed photometric decompositions, as judged by a global χ^2 figure-of-merit, for the 57 galaxies (38 from Sample A, 19 from Sample B) listed in Table 4. The latter includes the resulting bulge and disc structural parameters. Some examples illustrating the various fitting strategies are shown in Figure 3. These are the same galaxies, whose azimuthally-averaged surface brightness profiles are shown in Figure 2. For all of them, the ellipse-averaged radial profiles of surface brightness, ellipticity, and position angle of the model image are consistent with those measured on the galaxy image. The differences between model and data found in the ellipticity and position angle of NGC 4477 and in the ellipticity of NGC 3675 are due to the presence of a weak bar and strong dust lanes, respectively. These features are clearly seen in the galaxies' residual images. Nevertheless, the surface brightness residuals $\Delta\mu_i$ are remarkably small; $|\Delta\mu_i| < 0.2$ mag arcsec⁻² for all the galaxies shown in Figure 3, except for some portions of the dust lanes of NGC 3675 where the residuals increase to ~ 0.4 mag arcsec⁻². Although part of the NGC 3675 disc is missing, this does not affect the fit result. GASP2D performs a reliable fit as soon as the observed galaxy can be modelled by the sum of two axisymmetric components and the field of view covers at least half of the galaxy (Méndez-Abreu 2008).

The GASP2D formal errors obtained from the χ^2 minimisation method are not representative of the real errors in the structural parameters (Méndez-Abreu et al. 2008). Instead, the estimated errors given in Table 4 were obtained through a series of Monte Carlo simulations. To this end, we generated a set of 400 images of elliptical galaxies with a Sérsic spheroid and 400 images of disc galaxies with a Sérsic bulge and an exponential disc; each with a different PA and ellipticity. The range of tested parameters for the simulated images was taken from the photometric analysis of nearby elliptical galaxies by Kormendy et al. (2009) and face-on disc galaxies by Gadotti (2009) (but assuming a wider range of axial ratios than the latter). Our tests include treatment for resolution effects (galaxy distance, pixel scale, and seeing), colour effects (accounting for V and i bands), inclination, and more. The two-dimensional parametric decomposition was applied to analyse the images of the artificial galaxies as if they were real. The artificial and observed galaxies were divided in bins of 1 mag. The relative errors on the fitted parameters of the artificial galaxies were estimated by comparing the input and output values and were assumed to be normally distributed. In each magnitude bin, the mean and standard deviation of relative errors of artificial galaxies were adopted as the systematic and typical error on the relevant parameter for the observed galaxies. Overall, we find that GASP2D recovers the galaxy structural parameters with an uncertainty ranging from 1%, to 10%, and to 20% for brighter ($6.5 \leq m_{\text{tot},i} < 7.5$), intermediate ($10.5 \leq m_{\text{tot},i} < 11.5$), and fainter ($12.5 \leq m_{\text{tot},i} < 13.5$) sample galaxies, respectively.

The inclination of disc galaxies was calculated from the fitted disc axial ratio in the i -band as

$$\sin^2 i = \frac{1 - q_d^2}{1 - q_0^2}, \quad (3)$$

where q_0 is the intrinsic disc axial ratio. We obtain the latter from Paturel et al. (1997):

² Interactive Data Language is distributed by ITT Visual Information Solutions. It is available from <http://www.ittvis.com/>.

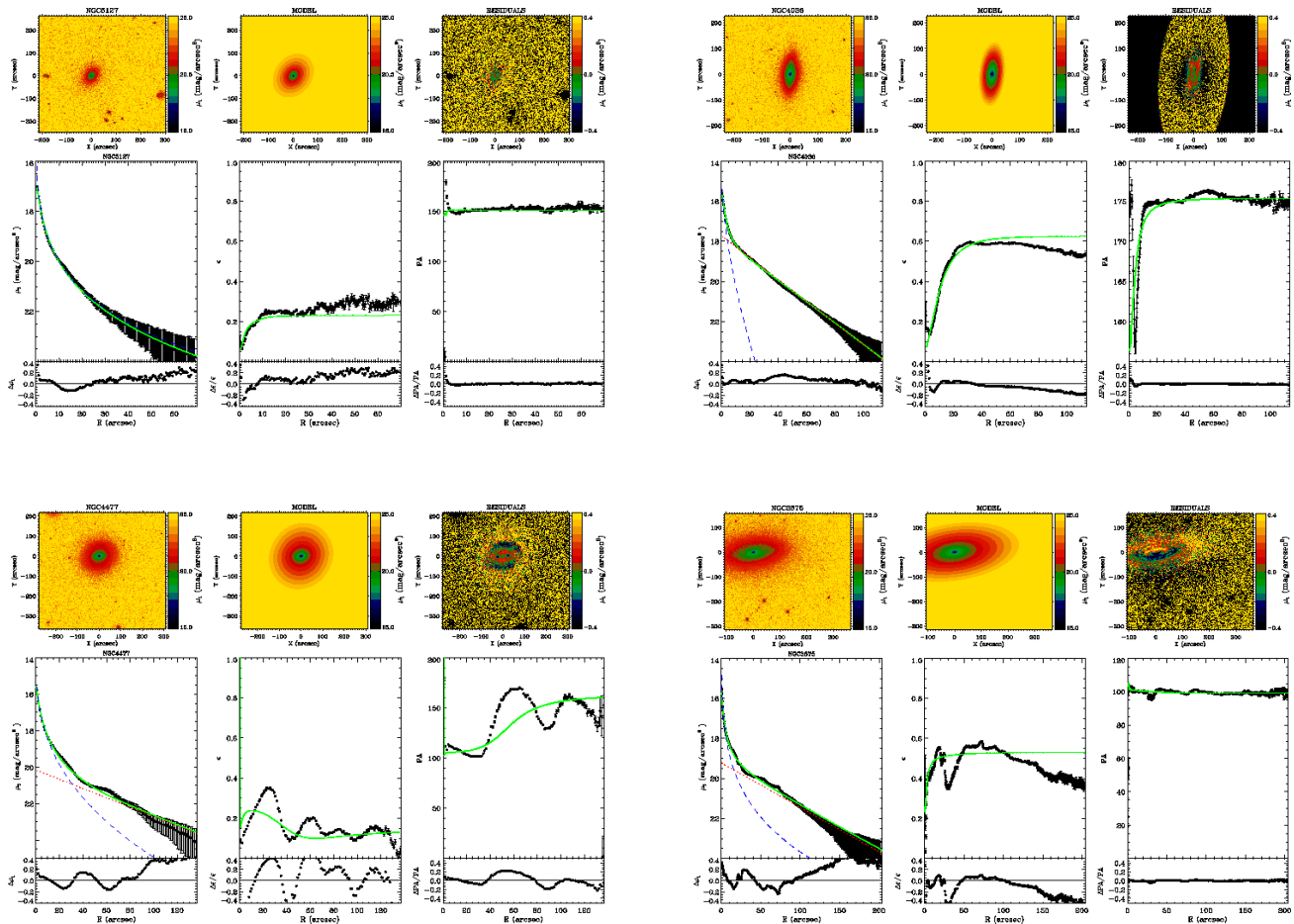


Figure 3. Two-dimensional photometric decomposition of the sample galaxies shown in Figure 2 illustrating the various fitting strategies adopted with GASP2D. For each galaxy, we show in the upper panels the SDSS i -band image (left), the best-fit image (middle), and the residual (i.e., observed-model) image (right). The lower panels show the ellipse-averaged radial profiles of the surface brightness (left), ellipticity (middle), and position angle (right) measured in the SDSS (dots) and model image (green continuous line). The difference between the ellipse-averaged radial profiles from the observed and model images are also shown. The dashed blue and dotted red lines represent the intrinsic surface brightness radial profiles of the bulge and disc, respectively. No disc contribution is assumed for the elliptical galaxy NGC 5127.

$$\log q_0 = -0.43 - 0.053 T, \quad (4)$$

where T is the galaxy Hubble type from RC3.

The fitted i -band disc axial ratios agree well with the isophotal axial ratios at a surface brightness level $\mu_B = 25$ mag arcsec $^{-2}$ reported in the RC3. Our disc axial ratios are on average 6% lower than RC3 with a standard deviation of 7%. We adopted the RC3 axial ratios for the lenticular and spiral galaxies whose GASP2D solution for the disc was too uncertain; this amounts to 28 galaxies in Sample A and another 8 in Sample B.

3.3 Stellar Velocity Dispersion

The measured stellar velocity dispersions, σ , for galaxies in Sample A were taken from the same sources as B09. We applied the aperture correction of Jørgensen et al. (1995) to transform the σ into the equivalent of an effective stellar dispersions, σ_e , measured within a circular aperture of radius $r_{e,\text{bulge}}$. The effective radii were also taken from the same sources as B09, except for the 35 galaxies for which $r_{e,\text{bulge}}$

was obtained from our own decomposition of the SDSS images (Tables 3 and 4). The maximum difference between our and literature values of $r_{e,\text{bulge}}$ is about 20%, though the comparison often involves different band passes which broadens the discrepancy.

The aperture correction was also applied to the σ measured for NGC 2892 and NGC 5921 by Ho et al. (2009) and Wegner et al. (2003), respectively.

For Sample B galaxies, we adopted the values of σ_e given by G09. These were derived as the luminosity-weighted mean of the stellar velocity dispersion within $r_{e,\text{bulge}}$.

3.4 Circular Velocity

The values for the galaxy circular velocity, V_c , for both elliptical and disc galaxies were collected from different sources.

We retrieved V_c from the compilation of Ho (2007) for 40 disc galaxies (31 from Sample A, 9 from Sample B). These were derived from the H I line widths available in the HyperLeda catalogue (Paturel et al. 2003). The W_{20} and W_{50}

line widths are measured at 20% and the 50% of the total H I line profile flux. For galaxies missing in Ho (2007), line widths were found in HyperLeda for an additional 27 galaxies (22 from the Sample A, 5 from Sample B). Given multiple sources in HyperLeda, we favoured the larger survey source for each galaxy in order to maximise the homogeneity of the data base³. All line widths were already corrected for instrumental resolution. We further applied a correction for cosmological stretching and broadening by gas turbulence following Bottinelli et al. (1983) and Verheijen & Sancisi (2001). Finally, the corrected line widths $W_{20,\text{corr}}$ and $W_{50,\text{corr}}$ were deprojected using the prescription of Paturel et al. (1997)

$$V_{20} = 0.5(10^{1.187 \log W_{20,\text{corr}} - 0.543}) / \sin i, \quad (5)$$

$$V_{50} = 0.5(10^{1.071 \log W_{50,\text{corr}} - 0.210}) / \sin i, \quad (6)$$

where the inclination, i , is listed in Table 1 and 2. We take the final circular velocity as the average of V_{20} and V_{50} ,

$$V_c = (V_{20} + V_{50})/2. \quad (7)$$

Following Ho (2007), we adopted a 5% error on V_c for the maximum velocity listed in HyperLeda.

For 14 early-type galaxies (7 in Sample A, 7 in Sample B), we adopted the value of V_c derived from dynamical modelling (IC 1459, Samurović & Danziger 2005; NGC 1052, Binney et al. 1990; NGC 3115, Bender et al. 1994; NGC 3608, Coccato et al. 2009; NGC 4314 Quillen et al. 1994; and 9 ellipticals in Kronawitter et al. 2000). For a few other galaxies (five in Sample A, one in Sample B), either the ionised-gas (NGC 2911, Sil'chenko & Afanasiev 2004; NGC 5252, Morse et al. 1998), the H I (IC 342, Pizzella et al. 2005; NGC 3801, Hota et al. 2009) or the CO kinematics (NGC 4526, Young et al. 2008), Milky Way (Baes et al. 2003) rotational velocity at large radii are assumed to represent V_c . We adopted a 10% error when the V_c uncertainty from models or observations was not given.

Finally, we eliminated 7 galaxies (4 from Sample A, 3 from Sample B) since their quoted circular velocities are unrealistically low (NGC 1497, NGC 3384, and NGC 5576, Paturel et al. 2003; NGC 3642, NGC 4429, NGC 5347, and NGC 7052, Ho 2007).

The final circular velocities of 88 galaxies from Sample A (65) and Sample B (23) are listed in Tables 1 and 2.

3.5 Masses

We estimated the bulge mass as $M_{\text{bulge}} = \alpha r_{e,\text{bulge}} \sigma_e^2 / G$, where G is the gravitational constant and $\alpha = 5.0 \pm 0.1$ (Cappellari et al. 2006) is a dimensionless constant that depends on galaxy structure. The effective radius, $r_{e,\text{bulge}}$, for elliptical galaxies is extracted from their azimuthally-averaged light profile (Table 3), whereas the bulge effective radius of lenticular and spiral galaxies is obtained from two-dimensional photometric decomposition (Table 4). In deriving M_{bulge} , we implicitly assumed that the measured value of σ_e is dominated by the bulge component. For late-type galaxies we expect that the disc contribution to σ_e results in an increase of the scatter of M_{bulge} as a function of the

morphological type. This does not affect our analysis since we could measure $r_{e,\text{bulge}}$ (and therefore M_{bulge}) for only a few Sb–Sbc galaxies. Moreover, the ratio $B/T > 0.1$ except for three galaxies.

Ferrarese et al. (2006) suggested a connection between M_\bullet and the mass of early-type galaxies calculated as

$$M_{e,\text{gal}} = \alpha r_{e,\text{gal}} \sigma_e^2 / G \text{ with } \alpha = 5.0 \pm 0.1. \quad (8)$$

Note that such a mass estimate is indicative of the galaxy mass within $r_{e,\text{gal}}$ and is thus an incomplete representation of the total galaxy mass. We calculated $M_{e,\text{gal}}$ for the elliptical and lenticular galaxies in our sample by adopting $r_{e,\text{gal}}$ calculated from the azimuthally-averaged light profiles (Table 3). For elliptical galaxies, $M_{\text{bulge}} = M_{e,\text{gal}}$. The virial estimator by Cappellari et al. (2006) captures the entire dynamical mass so long as total mass traces light (Thomas et al. 2011). Wolf et al. (2010) found a different coefficient ($\alpha = 4$) for their derivation of a mass estimator for stellar systems supported by velocity dispersion. The latter is a good estimate of the total dynamical mass inside a radius which is just larger than the effective radius (Thomas et al. 2011). The appropriate value of α is actually a function of the Sérsic shape index n (Trujillo et al. 2004; Cappellari et al. 2006). However the exact application of the $\alpha(n)$ relation, which results in a zero-point offset for $M_{e,\text{gal}}$, does not affect our conclusions. We thus make use of the Cappellari et al. (2006) mass estimator. Error estimates on M_{bulge} and $M_{e,\text{gal}}$ account for the uncertainty on α .

We derived the dynamical mass of the disc galaxies from

$$M_{\text{dyn}} = R V_c^2 / G, \quad (9)$$

where $R = r_{24.5}$ (Table 3). Most of the circular velocities that we derived from H I data yield no information about their radial coverage. Nevertheless, $M_{\text{dyn,gal}}$ corresponds to the galaxy mass within the optical radius, because $r_{24.5}$ is roughly indicative of the galaxy optical radius and the observations of spatially-resolved H I kinematics in spirals show that the size of H I discs closely matches that of a galaxy's optical disc (Ho et al. 2008a).

The masses computed from Eq. (8) and Eq. (9) are both available only for the 10 lenticular galaxies in our sample, since they share dynamical properties of both elliptical and spiral galaxies. For these galaxies, $\langle M_{\text{dyn,gal}} / M_{e,\text{gal}} \rangle = 1.27 \pm 0.07$.

The galaxy stellar masses, $M_{\star,\text{gal}}$, were derived from $L_{i,\text{gal}}$ under the assumption of constant mass-to-light ratio $(M/L)_i$. $(M/L)_i$ estimates were inferred from our $g-i$ colours following Bell et al. (2003). Their mass-to-light ratios were derived from the stellar population models of Bruzual & Charlot (2003), which are tuned to reproduce the ages and metallicities of the local spiral galaxies.

4 ANALYSIS

4.1 Correlations Between M_\bullet and Bulge and Galaxy Parameters

We used the data obtained in §3 to build scaling relations between M_\bullet and the bulge (i.e., the velocity dispersion, luminosity, virial mass, Sérsic index, and mean effective surface brightness) and galaxy (luminosity, circular velocity, stellar, virial, and dynamical mass) properties. In addition to

³ We selected the most recent and highest resolution observations available in the on-line HyperLeda catalogue (<http://leda.univ-lyon1.fr>) up to September 2009.

the Sample A+B, we also built a comparison sample with the 30 galaxies for which all the desired physical parameters could be measured. For each of the above parameters x , we assume that there exists a relation of the form

$$\log \frac{M_{\bullet}}{M_{\odot}} = \alpha + \beta \log \frac{x}{x_0} \quad (10)$$

where x_0 is a normalisation value chosen near the mean of the distribution of x -values.

The best-fit values of α and β , their associated uncertainties, the total scatter ϵ and intrinsic scatter ϵ_{intr} of the relation, the Spearman rank correlation coefficient ρ , and the level of significance of the correlation P were obtained as a function of the sample at hand. The results are given in Table 5. The quoted errors are all derived through a bootstrap technique.

Samples A+B and the comparison sample include both accurate determinations and upper limits of M_{\bullet} . The proper handling of these heterogeneous data sets requires that we perform a censored regression analysis (Feigelson & Nelson 1985; Isobe et al. 1986) with the ASURV⁴ package (Lavalley et al. 1992). Linear regressions were calculated with the EM maximum-likelihood algorithm implementing the technique of expectation (E-step) and maximization (M-step) by Dempster et al. (1977) which assumes normal residuals. For each relation, we checked that the distribution of residuals about the fitted line was normal. With uncensored data, this analysis would be equivalent to that of a standard least-squares linear regression. ASURV gives as correlation coefficient the generalised Spearman rank correlation coefficient ρ (Akritas 1989) and computes the level of significance of the correlation P . We derived the scatter of the relation ϵ as the root-mean square (rms) deviation in $\log(M_{\bullet}/M_{\odot})$ from the fitted relation assuming no measurement errors. This assumption does not affect our results, since we wish to compare the relative tightness of the different scaling relations for the comparison sample.

G09 focused their analysis on $M_{\bullet} - \sigma_e$ and $M_{\bullet} - L_{i,\text{bulge}}$. We have extended their analysis to a broader range of scaling relations by performing least-square linear regressions with the secure values of M_{\bullet} and the bulge and galaxy parameters measured for Sample B. We used the MPFITEXY⁵ algorithm (Williams et al. 2010), which accounts for measurement errors in both variables and the intrinsic scatter ϵ_{intr} of the relation. We used the IDL routine R_CORRELATE to compute the standard Spearman rank correlation coefficient ρ and the level of significance of the correlation. The intrinsic scatter of each relation was assessed by varying ϵ_{intr} in the fitting process to ensure that the reduced $\chi^2_{\nu} = 1$. The total scatter ϵ was derived as the rms deviation in $\log(M_{\bullet}/M_{\odot})$ from the fitted relation weighted by measurement errors.

In addition to fitting the M_{\bullet} -bulge and galaxy scaling relations as outlined above, we also look in the subsections below for correlations against morphological type or nuclear activity as listed in Tables 1 and 2. We will see that the latter (morphology or nuclear activity) do not play a strong

rôle in any of the M_{\bullet} -bulge and galaxy scaling relations. Morphology only plays a small rôle in the $M_{\bullet} - M_{\star,\text{gal}}$ and in the $M_{\bullet} - V_c$ relations.

4.1.1 M_{\bullet} versus σ_e

We have plotted the $M_{\bullet} - \sigma_e$ distribution for the Sample A+B in Figure 4. The slope of our $M_{\bullet} - \sigma_e$ relation is consistent within the errors with those by Ferrarese & Ford (2005) and Lauer et al. (2007) as discussed by B09, and with that by G09 by default. On the other hand, the inclusion of the upper limits measured by B09 and G09 slightly changes the zero point of the relation but does not appreciably affect its scatter. The $M_{\bullet} - \sigma_e$ relation is indeed the tightest correlation that we measure; its scatter is consistent with G09 ($\epsilon = 0.44 \pm 0.06$ dex) and slightly larger than Ferrarese & Ford (2005, $\epsilon = 0.34$ dex). According to G09, the increased fraction of spirals may be a source of the increased scatter with respect to previous estimates based mostly on SMBH measurements in early-type galaxies. Consistently, our analysis reveals that the $M_{\bullet} - \sigma_e$ scatter for late-type galaxies ($\epsilon = 0.52 \pm 0.14$ dex) alone is slightly larger than that of early-type galaxies ($\epsilon = 0.38 \pm 0.04$ dex). Nevertheless, at small σ_e , some upper limits exceed the expected M_{\bullet} as the line-widths for such low- σ_e outliers are most likely affected by the mass contribution of a conspicuous nuclear cluster (B09). The scatter for the late-type galaxies reduces to ($\epsilon = 0.38 \pm 0.05$ dex) by excluding the nucleated galaxies from the fit. Therefore, they are the cause for the observed difference between the scatter of early and late-type galaxies. We conclude that the $M_{\bullet} - \sigma_e$ relation is the same for both early and late-type galaxies. S0 galaxies overlap ellipticals at high σ_e values and spirals at low σ_e values.

Barred and unbarred galaxies follow the same $M_{\bullet} - \sigma_e$ relation within the errors. The same is not true for galaxies with classical and pseudo-bulge. We have classified our bulges according to their measured Sérsic index ($n > 2$ for classical and $n \leq 2$ for pseudo-bulges; Kormendy & Kennicutt 2004). We find slope differences in the $M_{\bullet} - \sigma_e$ relations of our 46 classical ($\beta = 3.86 \pm 0.71$) and 11 pseudo-bulges ($\beta = 5.63 \pm 0.86$), whereas their zero points ($\alpha = 8.09 \pm 0.09$ and $\alpha = 7.78 \pm 0.33$, respectively) are in closer agreement within the errors. Conversely, Hu (2008) found similar slopes and different zero points. At face values, our and Hu et al.'s correlation coefficients are in agreement. This is mostly due to the large error bars on the $M_{\bullet} - \sigma_e$ coefficients for pseudo-bulges, which translate into a lower level of significance of the $M_{\bullet} - \sigma_e$ relation for pseudo-bulges ($P < 2\%$) with respect to that for classical bulges ($P < 0.1\%$). This results supports the recent findings by Kormendy et al. (2011) that there is little or no correlation between M_{\bullet} and pseudo-bulges.

At high σ_e values, the M_{\bullet} of the Sample A+B shows a weak steepening with respect to $M_{\bullet} - \sigma_e$ confirming previous results by Wyithe (2006), Lauer et al. (2007), and Dalla Bontà et al. (2009).

Finally, Figure 4 shows the absence of trends of the $M_{\bullet} - \sigma_e$ relation with nuclear activity. The different types of nuclear activity cover all the σ_e range, with most LINERs at high σ_e and most Seyferts at low σ_e . This is expected considering the strong dependence of nuclear spectral class on Hubble type (and therefore on σ_e), with LINERs and

⁴ The FORTRAN source code of the Astronomy Survival Analysis Package (v.1.3) is available at <http://www2.astro.psu.edu/statcodes/asurv>.

⁵ The IDL source code of MPFITEXY is available at <http://purl.org/mike/mpfitexy/>.

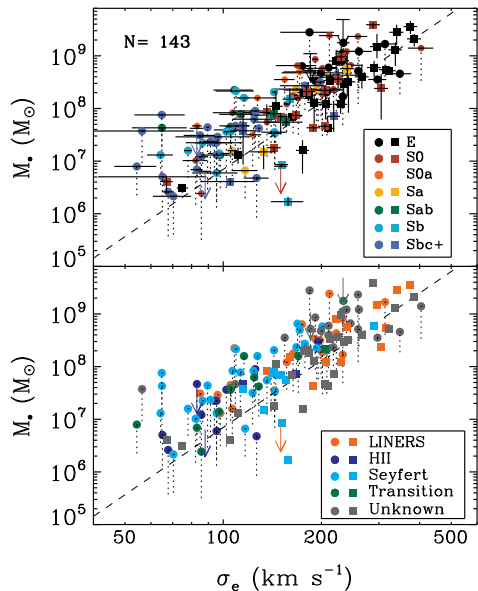


Figure 4. M_{\bullet} as a function of σ_e for 94 Sample A galaxies (89 upper limits from nebular line widths, circles; 5 upper limits from resolved kinematics, arrows) and 49 Sample B galaxies (squares). The total number of galaxies is $N = 143$. The error bars for σ_e are shown only in the upper panel for clarity. The lower and upper ends of the dotted lines correspond to M_{\bullet} upper limits estimated assuming an inclination of $i = 33^\circ$ and 81° for the unresolved Keplerian disc, respectively. Galaxies are plotted according to morphological type (upper panel) and nuclear activity (lower panel). The dashed line is the G09 $M_{\bullet} - \sigma_e$ relation. The Sbc+ bin includes all galaxies classified as Sbc or later.

Seyfert nuclei being more frequent in ellipticals and spirals, respectively (see Ho 2008, for a review).

4.1.2 M_{\bullet} versus $L_{i,\text{bulge}}$

The correlation between M_{\bullet} and the luminosity of the spheroidal component of a galaxy is also fairly tight (see Graham 2007, and references therein). Graham (2007) compared the different versions of the $M_{\bullet} - L_{\text{bulge}}$ by Kormendy & Gebhardt (2001), McLure & Dunlop (2002), Marconi & Hunt (2003), and Erwin et al. (2004). Recently, Sani et al. (2011) derived the $M_{\bullet} - L_{\text{bulge}}$ relation by measuring the $3.6 \mu\text{m}$ bulge luminosity. Since the differing relations do not predict the same SMBH mass, Graham (2007) investigated the effects of possible biases on the $M_{\bullet} - L_{\text{bulge}}$ relation including any dependency on the Hubble constant, the correction for dust attenuation in the bulges of disc galaxies, the mis-classification of lenticular galaxies as elliptical galaxies and the adopted regression analysis. These adjustments resulted in relations which are consistent with each other and suitable for predicting similar M_{\bullet} . In particular, a detailed photometric decomposition of the galaxy light profile is crucial to obtaining a representative bulge luminosity and therefore a reliable $M_{\bullet} - L_{\text{bulge}}$.

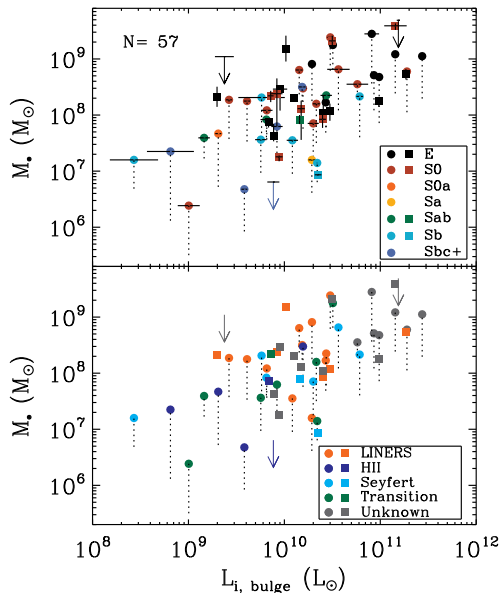


Figure 5. M_{\bullet} as a function of $L_{i,\text{bulge}}$ for 38 Sample A galaxies (35 upper limits from nebular line widths, circles; 3 upper limits from resolved kinematics, arrows) and 19 Sample B galaxies (squares) for which two-dimensional bulge-to-disc decompositions of the SDSS i -band images were performed. Symbols and panels are as in Figure 4.

G09 derived an updated value of the intrinsic scatter of the $M_{\bullet} - L_{\text{bulge}}$ relation, which is comparable to that of the $M_{\bullet} - \sigma_e$ relation in early-type galaxies, confirming the results of Marconi & Hunt (2003). According to them, the scatter of the $M_{\bullet} - L_{\text{bulge}}$ relation is significantly reduced when the bulge effective radius is extracted from a careful two-dimensional image decomposition.

Figure 5 shows our $M_{\bullet} - L_{i,\text{bulge}}$ relation. The best-fit coefficients are in agreement within the errors with Graham (2007) and Sani et al. (2011). The scatter is slightly higher than G09 who fit only early-type galaxies, but larger than that of the $M_{\bullet} - \sigma_e$ relation. All galaxies show a similar $M_{\bullet} - L_{i,\text{bulge}}$ distribution with no dependence on morphological type or nuclear activity. We cannot test the claim that barred and unbarred galaxies follow different $M_{\bullet} - L_{i,\text{bulge}}$ relations (Graham 2008; Graham & Li 2009; Gadotti & Kauffmann 2009; Hu 2009), since the sample galaxies with a strong bar were excluded for photometric decomposition and thus lack a $L_{i,\text{bulge}}$ measurement. For all the remaining galaxies, we did not model any other components than the bulge and disc (see Table 4).

4.1.3 M_{\bullet} versus M_{bulge}

The connection between the M_{\bullet} and L_{bulge} suggests a linear correlation with mass of the spheroidal component of the galaxy (Magorrian et al. 1998; McLure & Dunlop 2002; Marconi & Hunt 2003; Häring & Rix 2004).

The slope of our $M_{\bullet} - M_{\text{bulge}}$ relation (Fig. 6) is consistent within the errors with McLure & Dunlop (2002),

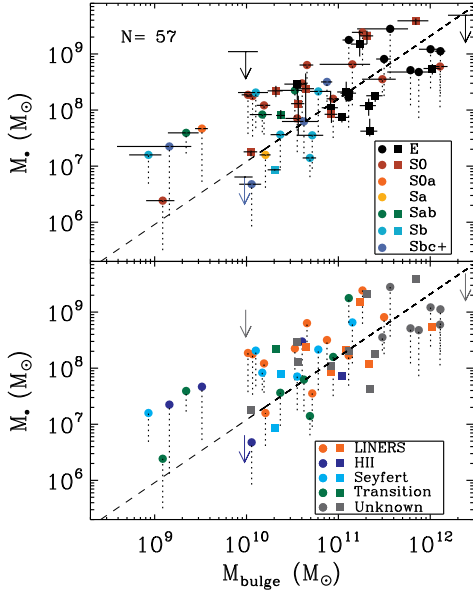


Figure 6. M_* as a function of M_{bulge} for the same sample as in Figure 5. Symbols and panels are as in Figure 4. The dashed line is the Häring & Rix (2004) $M_* - M_{\text{bulge}}$ relation.

Marconi & Hunt (2003), Aller & Richstone (2007) and Sani et al. (2011) and slightly shallower than Häring & Rix (2004). This regression is not a marked improvement over the $M_* - \sigma_e$ relation, as one might expect considering the additional fitting parameter in the mass measurement (namely the radius). Indeed, the $M_* - M_{\text{bulge}}$ is worse than the $M_* - \sigma_e$ relation. However, M_{bulge} is still a better proxy for M_* than $L_{i,\text{bulge}}$. Different Hubble types follow the same $M_* - M_{\text{bulge}}$ relation, with the lenticular galaxies covering the whole range of masses. There is also no dependence of this relation on nuclear activity, in agreement with McLure & Dunlop (2002).

4.1.4 M_* versus Sérsic n and $\langle \mu_{e,\text{bulge}} \rangle$

The two-dimensional photometric decompositions yield a panoply of galaxy structural parameters, including the Sérsic shape index n and mean effective surface brightness $\langle \mu_{e,\text{bulge}} \rangle$, both used as measure of the concentration of the bulge light. The Sérsic index n has indeed been adopted by some as a good tracer for M_* (Graham et al. 2001, 2003; Graham & Driver 2007).

Our $M_* - n$ relation (Figure 7) differs significantly from the linear and quadratic relations with $\log M_*$ and $\log n$ by Graham et al. (2001, 2003) and Graham & Driver (2007), respectively. In particular, the values of n for galaxies with high M_* are not as large as those in Graham & Driver (2007). The relation is characterised by a large scatter, small Spearman correlation coefficient, and low level of significance. Therefore, the correlation between M_* and n is poor and the $M_* - n$ relation is not reliable for predicting M_* . Our findings are in agreement with Hopkins et al. (2007b)

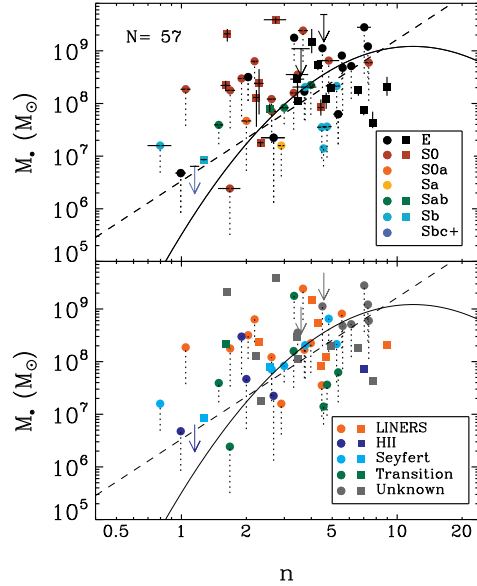


Figure 7. M_* as a function of n for the same sample as in Figure 5 for which two-dimensional bulge-to-disc decompositions of the SDSS i -band images were performed. Symbols and panels are as in Figure 4. The $M_* - n$ relations by Graham et al. (2001, 2003) and Graham & Driver (2007) are shown as the dashed and continuous lines, respectively.

who found no correlation between M_* and Sérsic index with both observations and hydrodynamical simulations.

The correlation between M_* and $\langle \mu_{e,\text{bulge}} \rangle$ (Figure 8) is also poor, lending further support to the idea that M_* is unrelated to the light concentration of the bulge, regardless of galaxy morphology and nuclear activity.

4.1.5 M_* versus $L_{i,\text{gal}}$

Kormendy (2001) compared the B -band total magnitude with dynamically secure M_* estimates in spheroids and few bulgeless disc galaxies. The poor correlation between M_* and $L_{i,\text{gal}}$ led him to conclude that the evolution of SMBHs is linked to bulges rather than discs.

We compared our own $L_{i,\text{gal}}$ with M_* as a function of the morphological type in Figure 9. The Spearman rank correlation coefficient suggests a correlation at 17% significance level, which is tighter than Kormendy (2001) but not as tight as that for the $M_* - L_{\text{bulge}}$ relation. Our sample is short of bulgeless galaxies which may explain the better agreement for our M_* and $L_{i,\text{gal}}$ with respect to Kormendy (2001). On the other hand, total and bulge luminosity differ for disc galaxies. The later the morphological type, the larger the discrepancy resulting in both a larger slope and scatter of the $M_* - L_{i,\text{gal}}$ relation with respect to $M_* - L_{\text{bulge}}$. The scatter is larger and the correlation weaker when the g -band total luminosity is considered. Our findings are consistent with Hu (2009, see their Fig. 6) and confirm that bulge luminosity is a better tracer of the mass of SMBHs than total light of the galaxy.

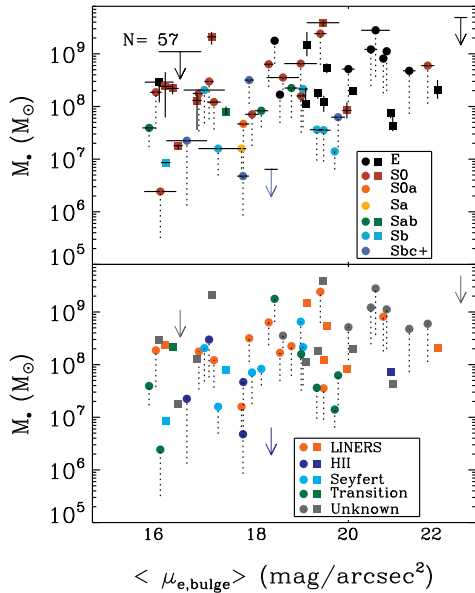


Figure 8. M_{\bullet} as a function of $\langle \mu_{e,\text{bulge}} \rangle$ for the same sample as in Figure 7. Symbols and panels are as in Figure 4.

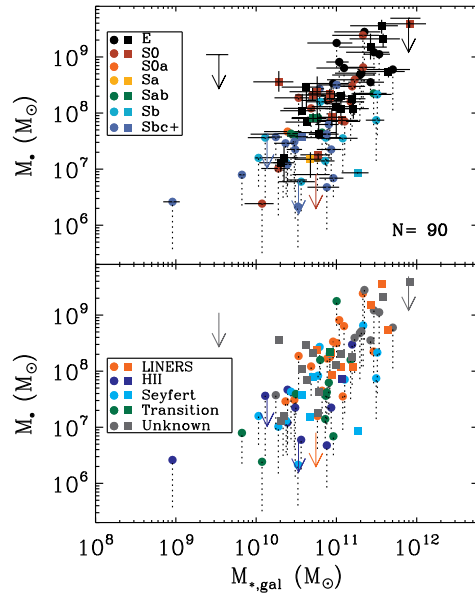


Figure 10. M_{\bullet} as a function of $M_{\star,\text{gal}}$ for the same sample as in Figure 9 for which $(g-i)$ colours from SDSS g and i -band images were derived. Symbols and panels are as in Figure 4.

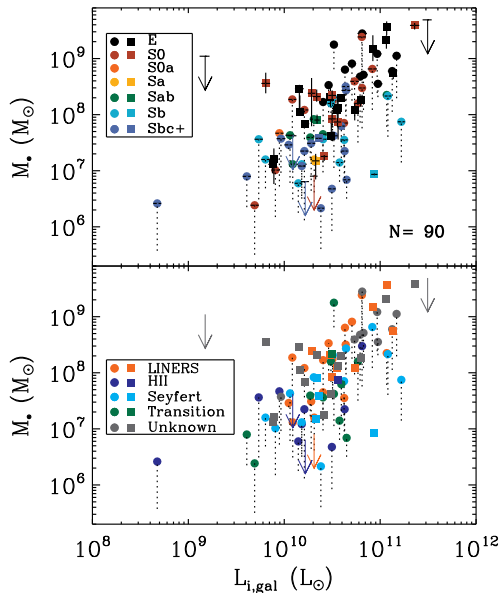


Figure 9. M_{\bullet} as a function of $L_{i,\text{gal}}$ for 62 Sample A galaxies (57 upper limits from nebular line widths, circles; 5 upper limits from resolved kinematics, arrows) and 28 Sample B galaxies (squares) for which azimuthally-averaged luminosity profiles from SDSS i -band images were extracted. Symbols and panels are as in Figure 4.

4.1.6 M_{\bullet} versus $M_{\star,\text{gal}}$, $M_{e,\text{gal}}$, and $M_{\text{dyn},\text{gal}}$

We have tested whether the scatter in predicting M_{\bullet} could be reduced by adopting $M_{\star,\text{gal}}$ rather than $L_{i,\text{gal}}$, since the galaxy luminosity is a proxy for its stellar mass. The $M_{\bullet} - M_{\star,\text{gal}}$ relation shown in Figure 10 is a slight improvement over the $M_{\bullet} - L_{i,\text{gal}}$ relation. The slopes are comparable but the Spearman rank correlation coefficient of the former is higher with a 3% significance level. Ellipticals and lenticulars follow a tighter $M_{\bullet} - M_{\star,\text{gal}}$ relation than late-type galaxies; the disc light clearly plays an anti-correlating rôle, indicating once more that the bulge parameters drive SMBH correlations.

We adopted the mass estimator from Cappellari et al. (2006) (i.e., the mass within the effective radius) for our ellipticals and lenticulars. The distribution of M_{\bullet} as a function of $M_{e,\text{gal}}$ for the early-type galaxies is plotted in Figure 11. They follow the same trend as the $M_{\bullet} - M_{e,\text{gal}}$ relation by Ferrarese et al. (2006). This is especially true for $M_{e,\text{gal}} > 10^{11} M_{\odot}$ where the fit slope and normalisation are consistent within the errors with Ferrarese et al. (2006). Less-massive galaxies seem to follow a steeper $M_{\bullet} - M_{e,\text{gal}}$ relation with a smaller normalisation. More data are however needed in this mass range to carefully address any trend differences. Introducing a new parameter $r_{e,\text{gal}}$ and a specific exponent for σ_e ought to considerably reduce the scatter of the $M_{\bullet} - \sigma_e$ relation but, in fact, it does not. In particular, the scatter of the $M_{\bullet} - \sigma_e$ relation is smaller than that of $M_{\bullet} - M_{e,\text{gal}}$ if the same sample of early-type galaxies is considered.

The dynamical mass $M_{\text{dyn},\text{gal}}$ (i.e., the mass within the optical radius) was taken as the galaxy mass estimator for lenticulars and spirals. It does not correlate with M_{\bullet} (Fig-

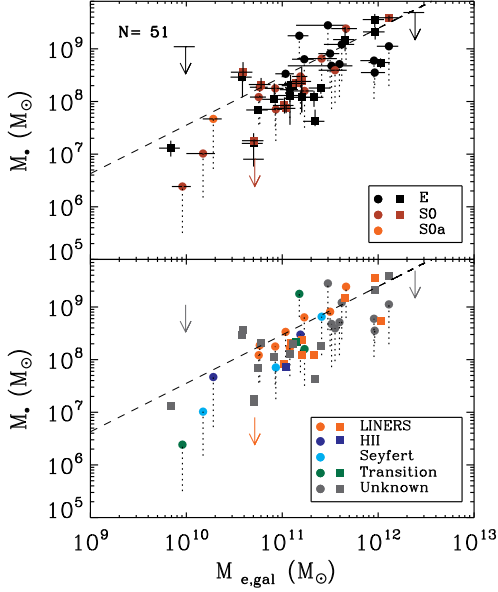


Figure 11. M_{\bullet} as a function of $M_{e,\text{gal}}$ for 27 Sample A galaxies (24 upper limits from nebular line widths, circles; 3 upper limits from resolved kinematics, arrows) and 24 Sample B galaxies (squares) ranging from E to S0a. Symbols and panels are as in Figure 4. The dashed line is the Ferrarese et al. (2006) $M_{\bullet}-M_{e,\text{gal}}$ relation.

ure 12), irrespective of Hubble type and nuclear activity. Our analysis reveals that the coarse $M_{\bullet}-M_{\text{dyn,gal}}$ relation found by Ho et al. (2008b, $\epsilon = 0.61$ dex) does not hold when galaxies with $M_{\text{dyn,gal}} \leq 10^{10} M_{\odot}$ (i.e., at the lower mass end of the $M_{\text{dyn,gal}}$ range) are taken into account. The scatter of the M_{\bullet} -galaxy mass relation is larger and the correlation weaker when $M_{\star,\text{gal}}$ and $M_{\text{dyn,gal}}$ are considered. Since the stellar and dynamical masses include the mass contribution of the disc component, we conclude that the bulge mass is a better tracer of M_{\bullet} . Nevertheless, the $M_{\bullet}-\sigma_e$ is tighter and yet again more fundamental than the $M_{\bullet}-M_{e,\text{gal}}$ relation.

4.1.7 $M_{\bullet}-V_c$ and $V_c-\sigma_e$ relations

Assuming that V_c at large radii trace the dark matter halo, we study the possible link between SMBHs and dark matter halos by comparing M_{\bullet} with V_c . A possible relation between M_{\bullet} and the dark matter depends clearly on the radius at which V_c is measured. Theoretical models that reproduce the observed luminosity function of quasars (Cattaneo 2001; Adams et al. 2003; Volonteri et al. 2003; Hopkins et al. 2005a; Springel et al. 2005) suggest that M_{\bullet} scales as a power law of the virial velocity (i.e., the circular velocity of the galactic halo at the virial radius) of the galactic halo of the SMBH host. However, the conversion between V_c measured at large radii and virial velocity, depends on the assumed model.

We show M_{\bullet} against V_c in Figure 13. There is a weak correlation between these quantities, which is mostly driven by the late-type galaxies.

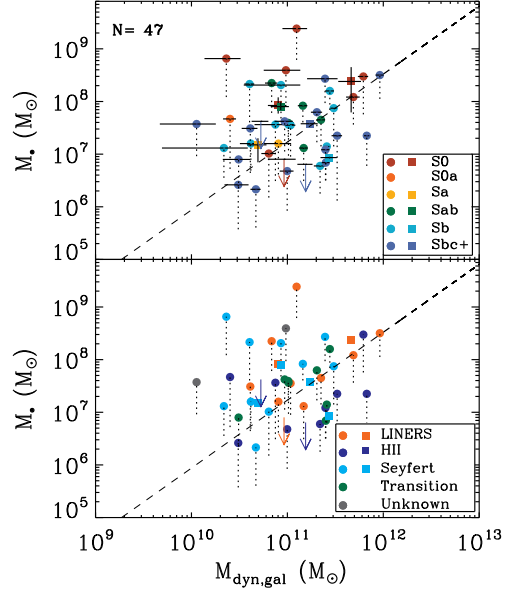


Figure 12. M_{\bullet} as a function of $M_{\text{dyn,gal}}$ for 41 Sample A disc galaxies (38 upper limits from nebular line widths, circles; 3 upper limits from resolved kinematics, arrows) and 6 Sample B (squares). Symbols and panels are as in Figure 4. The dashed line is the Ho et al. (2008b) $M_{\bullet}-M_{\text{dyn,gal}}$ relation.

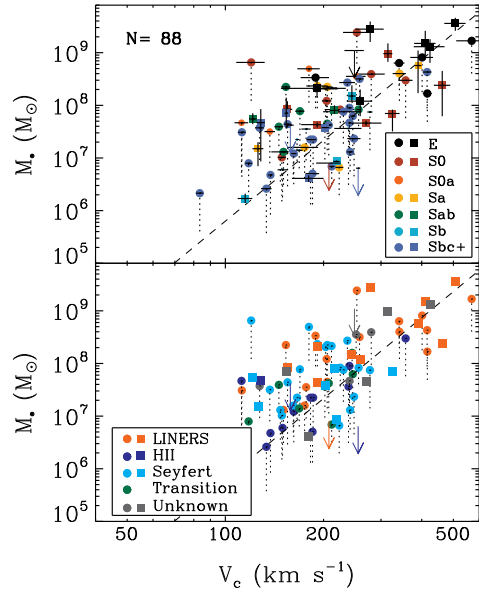


Figure 13. M_{\bullet} as a function of V_c for 65 Sample A disc galaxies (61 upper limits from nebular line widths, circles; 4 upper limits from resolved kinematics, arrows) and 23 Sample B galaxies (squares). Symbols and panels are as in Figure 4. The dashed line is the Ho (2007) $M_{\bullet}-V_c$ relation.

This is in agreement with previous studies by Zasov et al. (2005) and Ho et al. (2008b). Zasov et al. (2005) used a collection of 41 galaxies with M_\bullet , σ_e , and V_c from the literature to conclude that there is a coarse $M_\bullet - V_c$ relation and that, for a given V_c , early-type galaxies have larger M_\bullet than late-type galaxies. Ho et al. (2008b) studied the $M_\bullet - V_c$ relation for a sample of 154 nearby galaxies comprising both early and late-type systems for which M_\bullet was estimated from the mass-luminosity-line width relation (Kaspi et al. 2000; Greene & Ho 2005; Peterson & Bentz 2006) and V_c from HI and optical data (Ho et al. 2008a). They found that the correlation between M_\bullet and V_c improves if only the galaxies with the most reliable V_c measurements are considered. The distribution of our spiral galaxies is consistent with the $M_\bullet - V_c$ relation by Ho et al. (2008b), whereas the value of M_\bullet for elliptical and lenticular galaxies is almost constant over the full observed V_c range (Figure 13).

Ho et al. (2008b) suggested that the main source of scatter in the $M_\bullet - V_c$ relation is related to the dependence of V_c/σ_e on the bulge-to-disc ratio (Courteau et al. 2007; Ho 2007). Since the bulge-to-disc ratio scales with the light concentration (Doi et al. 1993), which is another way to estimate the degree of bulge dominance, we derived V_c/σ_e as a function of C_{28} . We found a general agreement with the relation found by Courteau et al. (2007). The Jeans equation evokes a relation between the circular velocity of galaxy and its velocity dispersion for a pressure-supported system. The V_c/σ_e relation was first reported by Whitmore et al. (1979) and more recently by Ferrarese (2002), Buyle et al. (2004), and Pizzella et al. (2005). Courteau et al. (2007) and Ho (2007) further demonstrated that the $V_c - \sigma_e$ relation must depend on a third parameter which depends on the galaxy structure.

The existence of the $M_\bullet - \sigma_e$ relation and the absence of a single universal $V_c - \sigma_e$ for all the morphological types is in contrast with the hypothesis that M_\bullet is more fundamentally connected to halo than to bulge, as suggested by Ferrarese (2002) and Pizzella et al. (2005). We conclude that the SMBH mass is associated with the bulge and not the halo (see also Peng 2010) by analysing the $V_c - \sigma_e$ relation as a function of M_\bullet for our sample galaxies (Figure 14). For a given M_\bullet , the range of V_c is on average 1.6 times larger than the range of σ_e demonstrating that M_\bullet is driven by σ_e and not by V_c . The few bulgeless galaxies known to host a SMBH (NGC 4395, Filippenko & Ho 2003; POX 52, Barth et al. 2004; NGC 1042, Shields et al. 2008) are an exception to this scenario, which is supported by cases like M33. The latter is a pure disc galaxy, which does not show any evidence of a SMBH (Gebhardt et al. 2001) but has a massive dark matter halo (Corbelli 2003).

More recently, Kormendy & Bender (2011) confirmed our early findings (Beifiori 2010) by extending the analysis of the $V_c - \sigma_e$ relation to bulgeless galaxies. They reported an absence of correlation between V_c and σ_e unless the galaxy also contains a bulge, suggesting that the fundamental driver for M_\bullet is σ_e for all Hubble types and that V_c plays only a small rôle in galaxies with a bulge. Although at this later cosmic time the $M_\bullet - V_c$ is coarser than the $M_\bullet - \sigma_e$ relation, Volonteri et al. (2011) remind us that a tighter connection in the past is not precluded. At earlier epochs, the SMBH assembly was more likely coupled to

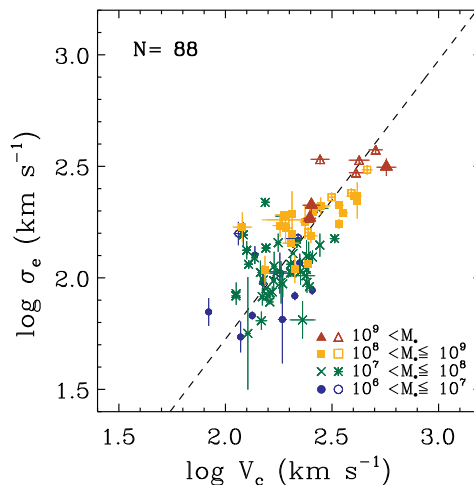


Figure 14. $V_c - \sigma_e$ relation as a function of M_\bullet for the same sample as in Figure 13. The dashed line is the Ho (2007) $V_c - \sigma_e$ relation.

the dark matter halo properties based on a merger-driven hierarchical formation scenario. Still, the scatter we measure for the $M_\bullet - V_c$ relation is a factor ~ 2 larger than that of the $M_\bullet - \sigma_e$ relation, which is significantly more than argued by Volonteri et al. (2011) in their analysis of Kormendy & Bender (2011)’s data set.

4.2 Correlations Between M_\bullet and Linear Combinations of Bulge and Galaxy Parameters

We wish to understand whether the relations between M_\bullet and bulge and galaxy properties studied in §4.1 can be improved by the addition of a third parameter. For the bulge or the galaxy parameters x and y in Table 6, a correlation of the form

$$\log \frac{M_\bullet}{M_\odot} = \gamma + \alpha \log \frac{x}{x_0} + \beta \log \frac{y}{y_0} \quad (11)$$

is assumed, where x_0 and y_0 are normalisation values chosen near the mean of the distribution of x and y values respectively. The fit parameters are the offset γ , and the logarithmic slopes α , β . The best-fit values of α , β , and γ , their associated uncertainties, the total scatter ϵ and intrinsic scatter ϵ_{intr} of the relation are given in Table 6. The Spearman rank test cannot be evaluated in the same way as described in §4.1 as it applies to two variables. To estimate the degree of correlations between the parameters in use, we applied the Spearman rank statistic using the projections of the planes once the combination of the two independent variables has been fixed to its best-fit values. This provides an indication of the degree of correlation between several linear combinations. The Spearman rank correlation coefficient ρ , and the significance of the correlation P derived for the projections are also given in Table 6. The quoted errors are all computed through a bootstrap technique.

For both Samples A+B and the comparison sample, we performed a censored regression analysis with two independent variables assuming normal residuals. The best-fit parameters were computed with the EM algorithm implemented in the ASURV package which yields maximum likelihood estimates from a censored data set allowing, in the general form, N observables distributed via a multivariate Gaussian distribution. We applied this technique to the special case of two independent variables and another dependent variable containing the censored data. The regression problem solves like a least-square fit but accounting for censored data. It uses initial guesses from an ordinary linear regression of the non-censored data and then converges on the new censored values.

The standard deviation is estimated in the standard fashion, weighted for a factor which accounts for the censored data (see Isobe et al. 1986, for details). The generalised Spearman rank correlation coefficient, and the significance of the correlation for the projections of planes, are based on the technique described in Akritas (1989). The total scatter was computed as the rms deviation in $\log(M_\bullet/M_\odot)$ from the fitted relation assuming no measurement errors.

We used our own modified version of the MPFITEXY algorithm to perform a least-squares linear regression of Sample B's data with two independent variables. Measurement errors were invoked in the derivation of best-fit parameters, total, and intrinsic scatter. The Spearman rank correlation coefficient and level of significance of the correlation were also derived by using the projections of the best-fit plane given all possible parameter combinations. The actual computation was done using the IDL routine R_CORRELATE.

4.2.1 M_\bullet versus Bulge Parameters

So far we have found that M_\bullet is more strongly related with σ_e than $L_{i,\text{bulge}}$ and M_{bulge} . Nevertheless, the correlation between the M_\bullet and M_{bulge} suggests that a possible combination of the bulge properties can result in a tighter correlation with M_\bullet . Note that the BHFP derives from the FP which connects $r_{e,\text{bulge}}$, σ_e , and $\langle\mu_{e,\text{bulge}}\rangle$ together (Dressler et al. 1987; Djorgovski & Davis 1987; Jørgensen et al. 2007, and reference therein). Therefore, we have analysed the residuals of $M_\bullet - \sigma_e$, $M_\bullet - L_{\text{bulge}}$, and $M_\bullet - M_{\text{bulge}}$ relations to test whether there is the evidence for an additional dependence with an additional parameter. The residuals were obtained as the difference between the observed data and their expected values from the fitting relations in Table 5. We compared the residuals in $\log(M_\bullet/M_\bullet[\sigma_e])$, $\log(M_\bullet/M_\bullet[L_{i,\text{bulge}}])$, and $\log(M_\bullet/M_\bullet[M_{\text{bulge}}])$ with the bulge photometric and kinematic properties (i.e., $\langle\mu_{e,\text{bulge}}\rangle$, $r_{e,\text{bulge}}$, n , and σ_e ; Figure 15). There is no trend between $\log(M_\bullet/M_\bullet[\sigma_e])$ and other bulge properties (Figure 15, left column), whereas $\log(M_\bullet/M_\bullet[L_{i,\text{bulge}}])$ and $\log(M_\bullet/M_\bullet[M_{\text{bulge}}])$ show a very weak dependence on $r_{e,\text{bulge}}$ according to the Spearman rank correlation coefficient and their significance intervals $\sim 6\%$ and $\sim 2\%$, respectively (Figure 15, middle and left columns, respectively). This was confirmed by Sani et al. (2011), who found no correlation of the residual with r_e .

We have tested for the more fundamental driver of M_\bullet .

To this aim we considered different linear combinations of the bulge parameters with M_\bullet (Figure 16). The correlation between M_\bullet , σ_e , and $r_{e,\text{bulge}}$ is as tight as the $M_\bullet - \sigma_e$ (Figure 16a). Taking into account $r_{e,\text{bulge}}$ does not significantly improve the $M_\bullet - \sigma_e$ fit. The relation between M_\bullet , $L_{i,\text{bulge}}$, and $r_{e,\text{bulge}}$ (Figure 16b) is not as strong as that between M_\bullet , σ_e , and $r_{e,\text{bulge}}$, but it is a slight improvement over $M_\bullet - L_{i,\text{bulge}}$. The relation between M_\bullet , σ_e , and $L_{i,\text{bulge}}$ is as tight as that between M_\bullet , σ_e , and $r_{e,\text{bulge}}$ (Figure 16c). The relation between M_\bullet , σ_e , and M_{bulge} (Figure 16d) is expected since M_{bulge} is known to correlate with M_\bullet and it depends on both σ_e and $r_{e,\text{bulge}}$. For this reason the two correlations with M_\bullet and either σ_e and M_{bulge} or $r_{e,\text{bulge}}$ and M_{bulge} are different (but not independent) expressions of the same relationship. Thus, larger SMBHs are associated with more massive and larger bulges, as understood in the framework of coevolution of spheroids and SMBHs. Hopkins et al. (2007a,b) first studied the residuals of the $M_\bullet - M_{\text{bulge}}$ and $M_\bullet - \sigma_e$ relations with bulge properties, finding tighter correlations between the combination of the bulge parameters and M_\bullet . This bolstered the notion of a BHFP. The bulge parameters M_{bulge} and $L_{i,\text{bulge}}$ are indeed physically related to each other through the fundamental plane relation (FP) and virial theorem. The existence of such BHFP has important implications for the largest M_\bullet and resolves the apparent conflict between expected and measured values of M_\bullet for the outliers in both $M_\bullet - \sigma_e$ and $M_\bullet - M_{\text{bulge}}$ relations (e.g. Bernardi et al. 2007; Lauer et al. 2007). A similar correlation, but between M_\bullet , $r_{e,\text{bulge}}$, and $\langle\mu_{e,\text{bulge}}\rangle$, was reported by Barway & Kembhavi (2007) for nearby ellipticals with measured M_\bullet . This correlation has a smaller scatter than the $M_\bullet - \sigma_e$ and $M_\bullet - L_{\text{bulge}}$ relations and gives further support to the existence of a FP-type relation for SMBHs.

Furthermore, by comparing the tightness of the correlations between M_\bullet and linear combination of the bulge parameters, we argue that σ_e is the parameter that drives the connection with M_\bullet in the BHFP. A small contribution is due to $r_{e,\text{bulge}}$ or $L_{i,\text{bulge}}$. Similar results were obtained by Aller & Richstone (2007) who compared M_\bullet with σ_e , $I_{e,\text{bulge}}$ and $r_{e,\text{bulge}}$. Thus, including an additional parameter to the relation does not improve the quality of the fit, with σ_e always being the dominant parameter.

4.2.2 M_\bullet versus Galaxy Parameters

We also wish to test if the shallow $M_\bullet - L_{i,\text{gal}}$ and $M_\bullet - M_{\star,\text{gal}}$ relations can be improved by the addition of another galaxy parameter. Therefore, we calculated the residuals of $M_\bullet - \sigma_e$, $M_\bullet - L_{i,\text{gal}}$, and $M_\bullet - M_{\star,\text{gal}}$ relations to look for the signature of an additional galaxy parameter. The residuals were obtained as the difference between the data points and the relation fits listed in Table 5. We compared the residuals in $\log(M_\bullet/M_\bullet[\sigma_e])$, $\log(M_\bullet/M_\bullet[L_{i,\text{gal}}])$, and $\log(M_\bullet/M_\bullet[M_{\star,\text{gal}}])$ with the galaxy photometric and kinematic properties (i.e., C_{28} , $I_{e,\text{gal}}$, $r_{e,\text{gal}}$, and σ_e ; Figure 17). For $\log(M_\bullet/M_\bullet[\sigma_e])$, no trends with other galaxy properties are found whereas the $\log(M_\bullet/M_\bullet[L_{i,\text{gal}}])$ and $\log(M_\bullet/M_\bullet[M_{\star,\text{gal}}])$ relations show a weak dependence on r_e according to the Spearman rank correlation coefficient with a significance levels of 0.3% and 0.9%, respectively. We also examined the residuals of the $M_\bullet - (g - i)$ relation to check that our results are not affected by the propagated errors in

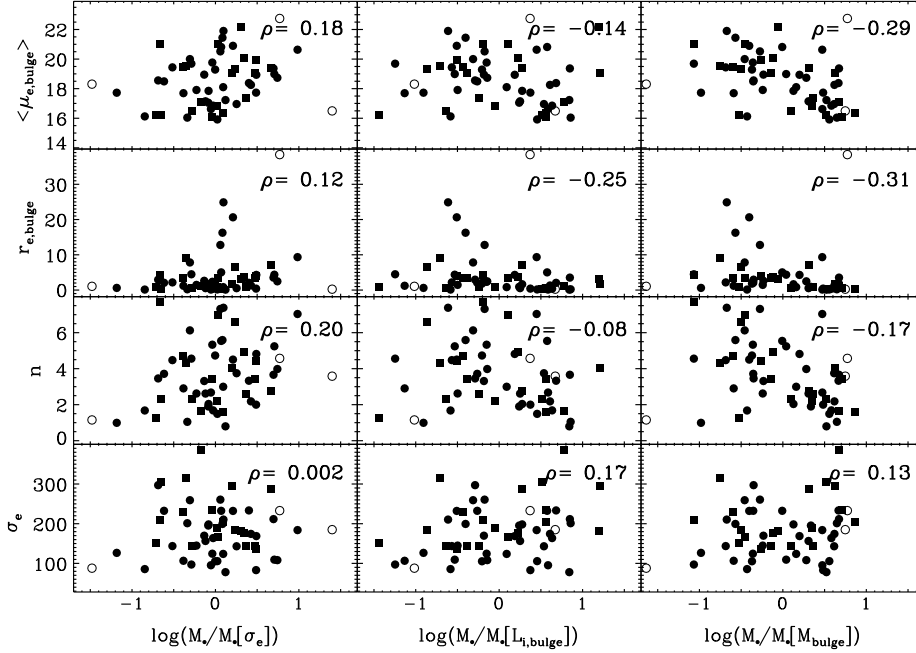


Figure 15. Residuals of the $M_\bullet - \sigma_e$, $M_\bullet - L_{i,\text{bulge}}$, $M_\bullet - M_{\text{bulge}}$ relations versus $\langle \mu_{e,\text{bulge}} \rangle$, $r_{e,\text{bulge}}$, n , σ_e for 38 Sample A galaxies (35 upper limits from nebular line widths, filled circles; 3 upper limits from resolved kinematics, open circles) and 19 Sample B galaxies (squares). The total number of galaxies is $N = 57$. The Spearman rank correlation coefficient ρ is given in each panel.

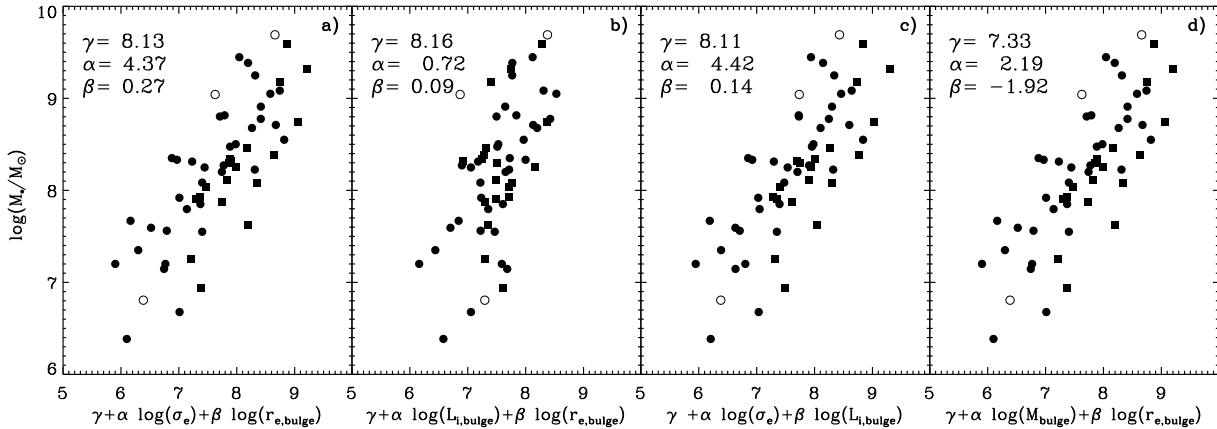


Figure 16. M_\bullet as a function of σ_e and $r_{e,\text{bulge}}$ (a), $L_{i,\text{bulge}}$ and $r_{e,\text{bulge}}$ (b), σ_e and $L_{i,\text{bulge}}$ (c), M_{bulge} and $r_{e,\text{bulge}}$ (d) for the same sample as in Figure 15. The logarithmic slopes α and β and offset γ of the fitted relation are given in each panel.

the determination of $M_{\star,\text{gal}}$. Figure 18 shows the different linear combinations of two galaxy parameters with M_\bullet . A few tight correlations are found when considering the total galaxy rather than bulge parameters. The tightness always depends on having σ_e as a fitting parameter (Table 6), i.e., the Spearman rank correlation coefficient is higher when σ_e is taken into account. The constancy of the Spearman rank

correlation coefficient despite the addition of other fitting parameters, argues that the main acting parameter is σ_e .

We conclude that the addition of bulge (e.g., $r_{e,\text{bulge}}$, $L_{i,\text{bulge}}$, M_{bulge}) or galaxy (e.g., $r_{e,\text{gal}}$, $L_{i,\text{gal}}$, $M_{\star,\text{gal}}$) structural parameters does not appreciably modify and improve the $M_\bullet - \sigma_e$ relation. We exclude that parameter covariances would produce the same scatter in both the $M_\bullet - \sigma_e$ and $M_\bullet - \sigma_e - r_e$ relations. Such a conspiracy would require

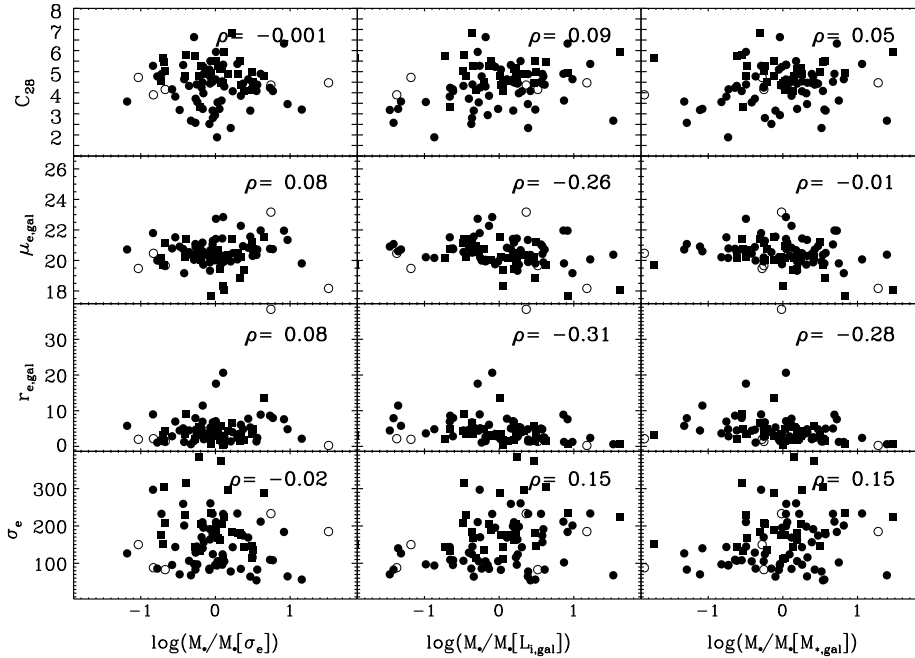


Figure 17. Residuals of the M_* – σ_e , M_* – $L_{i,gal}$, M_* – $M_{*,gal}$ relations versus C_{28} , $I_{e,gal}$, $r_{e,gal}$, σ_e for 62 Sample A galaxies (57 upper limits from nebular line widths, filled circles; 5 upper limits from resolved kinematics, open circles) and 28 Sample B galaxies (squares). The total number of galaxies is $N = 90$. The Spearman rank correlation coefficient ρ is given in each panel.

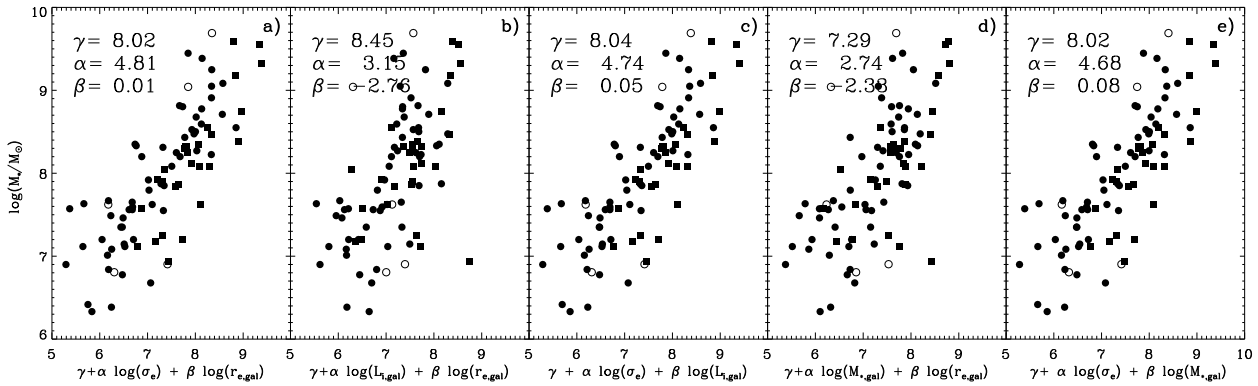


Figure 18. M_* as a function of σ_e and $r_{e,gal}$ (a), $L_{i,gal}$ and $r_{e,gal}$ (b), σ_e and $L_{i,gal}$ (c), $M_{*,gal}$ and $r_{e,gal}$ (d), and σ_e and $M_{*,gal}$ (e) for the same sample as in Figure 17. The logarithmic slopes α and β and offset γ of the fitted relation are given in each panel.

an anti-correlation between σ_e and $r_{e,bulge}$ (or $r_{e,gal}$) which is not observed.

5 DISCUSSION

The existence of the M_* scaling relations implies that SMBH and galaxy formation processes are closely linked. Some of the challenges of the current models of SMBH formation and evolution include reproducing and maintaining the re-

lations regardless of the sequence of galaxy evolution during the hierarchical mass assembly (Robertson et al. 2006a; Schawinski et al. 2006; Croton 2009). A more comprehensive assessment the M_* scaling relations scatter thus enables a better characterisation of the different SMBH/galaxy formation models.

Our large sample of galaxies with secure determination or upper limits of M_* has enabled a thorough investigation of the SMBH demography over a wide range of M_* , morphological type, and nuclear activity. After establishing the

unbiased mapping of M_\bullet upper limits against that of secure M_\bullet , we tested whether M_\bullet is more fundamentally driven by one of the several bulge (i.e., the velocity dispersion, luminosity, virial mass, Sérsic index, and mean effective surface brightness) and galaxy (luminosity, circular velocity, stellar, virial, and dynamical mass) parameters known to correlate with the SMBH mass, and if the known scaling relations can be improved with the addition of a third parameter.

- We argue that M_\bullet is fundamentally driven by σ_e , considering that the $M_\bullet - \sigma_e$ relation has the tightest scatter with respect to all other scaling relations. The scatter of our $M_\bullet - \sigma_e$ relation is comparable to G09 but slightly larger than that of Ferrarese & Ford (2005). At small σ_e , some M_\bullet upper limits exceed the expectation value as they likely account for the mass of a conspicuous nuclear cluster (B09). Excluding these galaxies from the fit reduces the scatter to Ferrarese & Ford (2005)'s value. Barred and unbarred galaxies as in B09 and G09 follow the same $M_\bullet - \sigma_e$ relation within the errors, contrary to Graham (2008)'s findings. Classical and pseudo-bulges were identified according to their Sérsic index (Kormendy & Kennicutt 2004). The $M_\bullet - \sigma_e$ relations of classical and pseudo-bulges have a different slope. The low significance of the $M_\bullet - \sigma_e$ relation for pseudo-bulges is in agreement with more recent findings by Kormendy et al. (2011) and suggests that the formation and growth histories of SMBHs depend on the host bulge type.

- The $M_\bullet - L_{i,\text{bulge}}$ relation is clearly not as tight as the $M_\bullet - \sigma_e$ one. However, the fact that G09 found a $M_\bullet - L_{i,\text{bulge}}$ relation as tight as the $M_\bullet - \sigma_e$ one is not in contradiction with our results, since G09 accounted only for early-type galaxies. The same is true for the $M_\bullet - M_{\text{bulge}}$ correlation, although the bulge mass proved to be a better proxy of M_\bullet than L_{bulge} and it includes $r_{e,\text{bulge}}$ as an additional fitting parameter.

- Contrary to previous findings (Graham et al. 2001, 2003; Graham & Driver 2007), we find little or no correlation between M_\bullet and Sérsic n in agreement with Hopkins et al. (2007b). The latter stated that M_\bullet is unrelated with the light concentration of the bulge based on observations and simulations. Consistently, we confirm that M_\bullet and $\langle \mu_{e,\text{bulge}} \rangle$ are poorly correlated.

- The correlations between M_\bullet and galaxy luminosity or mass are not a marked improvement over the $M_\bullet - \sigma_e$ relation. These scaling relations are strongly sensitive to the morphology of the host galaxies, with the presence of a disc playing an anti-correlating rôle, as first pointed out by (Kormendy 2001). This is a further indication that bulges are driving the SMBH correlations and SMBH evolution.

- We found that the $M_\bullet - V_c$ relation is significantly coarser than that of the $M_\bullet - \sigma_e$ relation, with a scatter about twice larger, suggesting that M_\bullet is more strongly controlled by the baryons than the dark matter.

- To assess the need for an additional parameter in the M_\bullet -bulge/galaxy scaling relations, we performed both a residual analysis and third-parameter fits as in Hopkins et al. (2007b), Barway & Kembhavi (2007), and Aller & Richstone (2007). To this aim we considered different linear combinations of bulge or galaxy parameters with M_\bullet . The strongest correlations always include σ_e as a fundamental structural parameter. The tightest relation is found between M_\bullet , σ_e , and $r_{e,\text{bulge}}$ (also known as the

BHFP, Hopkins et al. 2007a,b). Since its scatter does not change appreciably compared to that of the $M_\bullet - \sigma_e$ relation, the addition of $r_{e,\text{bulge}}$ is barely an improvement. This is a further confirmation that σ_e is the fundamental parameter which drives also the BHFP.

Our findings about the tightness of scaling relations such as the $M_\bullet - \sigma_e$ may be interpreted in the framework of self-regulating feedback in galaxies Hopkins et al. (2009). These authors argued that the energy released from the accretion of gas onto a SMBH is enough to stop further gas accretion, drive away the gas, and quench star formation. Hopkins et al. (2009) studied the relation between M_\bullet and the mass of the gas accreting onto the SMBH as a function of the distance from the central engine. The scatter of the M_\bullet -stellar mass relation increases at smaller radii (i.e., approaching the radius of influence of the SMBH) and decreases at larger radii (i.e., where the SMBH scaling relations are defined). This has been interpreted in terms of self-regulated growth of SMBHs, where the SMBH accretes and regulates itself without accounting for the gas supply but just being controlled by the bulge properties.

In this scenario, σ_e is the property which gives the tightest connection with MBH since it determines the depth of the local potential well from which the gas must be expelled. Younger et al. (2008) studied self-regulated models of SMBHs growth in different scenarios of major mergers, minor mergers, and disc instabilities, to find that SMBHs depend on the scale at which self-regulation occurs. They compared the bulge binding energy and total binding energy with M_\bullet , finding that the total binding energy is not a good indicator of M_\bullet mass in disc-dominated systems. This agrees with our findings that the late-type systems deviate most significantly from the M_\bullet -galaxy and BHFP scaling relations.

Several SMBH formation models predict a connection between M_\bullet and the total mass of the galaxy (Haehnelt et al. 1998; Silk & Rees 1998; Adams et al. 2001; Croton et al. 2006; Croton 2009) such that if the dark and baryonic matter act to form the bulge and SMBH, the dark halo determines the bulge and SMBH properties. Therefore, the mass of the SMBH and dark matter halo should be connected (Cattaneo 2001; Hopkins et al. 2005a,b). Numerous recent studies have erred along those lines. For instance, Bandara et al. (2009) studied the correlation between M_\bullet and total (luminous+dark) mass of the galaxy estimated from numerical simulations of gravitational lensing. Their relation suggests that the more massive halos are more efficient at forming SMBHs than the less massive ones; the slope of their relation suggests merger-driven, feedback-regulated processes of SMBH growth. Likewise, Booth & Schaye (2010) used self-consistent simulations of the coevolution of SMBHs and galaxies to confirm the relation by Bandara et al. (2009) and to prove that self-regulation of the SMBH growth occurs on dark matter halo scales. Volonteri & Natarajan (2009) investigated through numerical simulations the observational signature of the self-regulated SMBH growth by analysing the mass assembly history of black hole seeds. They found that the $M_\bullet - \sigma_e$ relation stems from the merging history of massive dark halos, and that its slope and scatter depend on the halo seed and specific SMBH self-regulation process.

Our observational results are not supportive of such results. We found only a weak correlation of M_{\bullet} with V_c . This agrees with our expectations based on the observed tightness of the $M_{\bullet} - \sigma_e$ relation and given the fact that the scatter of the $V_c - \sigma_e$ relation is large and morphologically-dependent (Courteau et al. 2007; Ho 2007).

The $M_{\bullet} - V_c$ relation may be improved with homogeneous measurements of the V_c data base. Indeed, while our collection of observed velocities is as current and reliable as possible, especially for spiral galaxies, we still lack a fully homogeneous data base. Many of us are working on improvements of this nefarious situation. However it is clear, as this work demonstrates, that the $M_{\bullet} - \sigma$ is the definitive fundamental relation of the SMBH-bulge connection.

ACKNOWLEDGEMENTS

We are indebted to Ralf Bender, Michele Cappellari, Lodovico Coccatto, Elena Dalla Bontà, Victor Debattista, John Kormendy, Tod Lauer, Lorenzo Morelli, Alessandro Pizzella, Marc Sarzi, and Roberto Saglia for many useful discussions and suggestions. We also thank Jairo Méndez Abreu for his GASP2D package which we used to measure the photometric parameters of our sample galaxies. We acknowledge the anonymous referee for valuable comments that led to an improved presentation. AB is grateful to Queen’s University for its hospitality while part of this paper was being written. AB was also supported by a grant from Accademia dei Lincei and Royal Society as well as STFC rolling grant ST/I001204/1 “Survey Cosmology and Astrophysics”. EMC was supported by Padua University through grants CPDA089220/08 and CPDR095001/09 and by Italian Space Agency through grant ASI-INAF I/009/10/0. SC and YZ acknowledge support from the Natural Science and Engineering Science Council of Canada. This research has made use of the HyperLeda database, NASA/IPAC Extragalactic Database (NED), and Sloan Digital Sky Survey (SDSS).

REFERENCES

- Abazajian, K. N. et al. 2009, *ApJS*, 182, 543
- Adams F. C., Graff D. S., Mbonye M., Richstone D. O., 2003, *ApJ*, 591, 125
- Adams F. C., Graff D. S., Richstone D. O., 2001, *ApJ*, 551, L31
- Aihara, H., et al. 2011, *ApJS*, 193, 29
- Akritas M., 1989, Technical Reports and Preprints Series 87. Dept. Statistics, Penn State University, Philadelphia
- Aller M. C., Richstone D. O., 2007, *ApJ*, 665, 120
- Baes M., Buyle P., Hau G. K. T., Dejonghe H., 2003, *MNRAS*, 341, L44
- Bandara K., Crampton D., Simard L., 2009, *ApJ*, 704, 1135
- Barth A. J., Ho L. C., Rutledge R. E., Sargent W. L. W., 2004, *ApJ*, 607, 90
- Barway S., Kembhavi A., 2007, *ApJ*, 662, L67
- Beifiori A., 2010, PhD thesis, Università di Padova
- Beifiori A., Sarzi M., Corsini E. M., Dalla Bontà E., Pizzella A., Coccato L., Bertola F., 2009, *ApJ*, 692, 856 (B09)
- Bell E. F., McIntosh D. H., Katz N., Weinberg M. D., 2003, *ApJS*, 149, 289
- Bender R., Saglia R. P., Gerhard O. E., 1994, *MNRAS*, 269, 785
- Bernardi M., Hyde J. B., Sheth R. K., Miller C. J., Nichol R. C., 2007, *AJ*, 133, 1741
- Bernardi M., Sheth R. K., Tundo E., Hyde J. B., 2007, *ApJ*, 660, 267
- Binney J. J., Davies R. L., Illingworth G. D., 1990, *ApJ*, 361, 78
- Blanton M. R., Kazin E., Muna D., Weaver B. A., Price-Whelan A., 2011, *AJ*, 142, 31
- Booth C. M., Schaye J., 2010, *MNRAS*, 405, L1
- Bottinelli L., Gouguenheim L., Paturel G., de Vaucouleurs G., 1983, *A&A*, 118, 4
- Bruzual G., Charlot S., 2003, *MNRAS*, 344, 1000
- Buyle P., Baes M., Dejonghe H., 2004, in Ryder S., Pisano D., Walker M., Freeman K., eds, *IAU Symp. 220, Dark Matter in Galaxies*. Astron. Soc. Pac., San Francisco, p. 317
- Caon N., Capaccioli M., D'Onofrio M., 1993, *MNRAS*, 265, 1013
- Cappellari M., et al. 2006, *MNRAS*, 366, 1126
- Cattaneo A., 2001, *MNRAS*, 324, 128
- Coccato L., et al. 2009, *MNRAS*, 394, 1249
- Corbelli E., 2003, *MNRAS*, 342, 199
- Courteau S., de Jong R. S., Broeils A. H., 1996, *ApJ*, 457, L73
- Courteau S., McDonald M., Widrow L. M., Holtzman J., 2007, *ApJ*, 655, L21
- Cox T. J., Dutta S. N., Di Matteo T., Hernquist L., Hopkins P. F., Robertson B., Springel V., 2006, *ApJ*, 650, 791
- Croton D. J., 2009, *MNRAS*, 394, 1109
- Croton D. J., et al. 2006, *MNRAS*, 365, 11
- Dalla Bontà E., Ferrarese L., Corsini E. M., Miralda-Escudé J., Coccato L., Sarzi M., Pizzella A., Beifiori A., 2009, *ApJ*, 690, 537
- de Vaucouleurs G., de Vaucouleurs A., Corwin Jr. H. G., Buta R. J., Paturel G., Fouque P., 1991, *Third Reference Catalogue of Bright Galaxies (RC3)*. Springer-Verlag, Berlin
- Debatista V. P., Corsini E. M., Aguerri J. A. L., 2002, *MNRAS*, 332, 65
- Dempster A. P., Laird N. M., Rubin D. B., 1977, *J. Roy. Stat. Soc. B*, 39, 1
- Di Matteo T., Springel V., Hernquist L., 2005, *Nature*, 433, 604
- Djorgovski S., Davis M., 1987, *ApJ*, 313, 59
- Doi M., Fukugita M., Okamura S., 1993, *MNRAS*, 264, 832
- Donzelli C. J., Chiaberge M., Macchetto F. D., Madrid J. P., Capetti A., Marchesini D., 2007, *ApJ*, 667, 780
- Dressler A., 1989, in Osterbrock D. E. & Miller J. S. eds., *IAU Symp. 134 Active Galactic Nuclei*, p. 217
- Dressler A., Lynden-Bell D., Burstein D., Davies R. L., Faber S. M., Terlevich R., Wegner G., 1987, *ApJ*, 313, 42
- Erwin P., Graham A. W., Caon N., 2004, in Ho L. C., ed, *Coevolution of Black Holes and Galaxies*. Carnegie Observatories, Pasadena, p. 12
- Feigelson E. D., Nelson P. I., 1985, *ApJ*, 293, 192
- Feoli A., Mancini L., 2009, *ApJ*, 703, 1502
- Ferrarese L., 2002, *ApJ*, 578, 90
- Ferrarese L., et al. 2006, *ApJ*, 644, L21
- Ferrarese L., Ford H., 2005, *Space Sci. Rev.*, 116, 523
- Ferrarese L., Merritt D., 2000, *ApJ*, 539, L9
- Filippenko A. V., Ho L. C., 2003, *ApJ*, 588, L13
- Freedman W. L., et al. 2001, *ApJ*, 553, 47
- Freeman K. C., 1970, *ApJ*, 160, 811
- Gadotti D. A., 2009, *MNRAS*, 393, 1531
- Gadotti D. A., Kauffmann G., 2009, *MNRAS*, 399, 621
- Gebhardt K., et al. 2000, *ApJ*, 539, L13
- Gebhardt K., et al. 2001, *AJ*, 122, 2469
- Graham A. W., 2007, *MNRAS*, 379, 711
- Graham A. W., 2008, *ApJ*, 680, 143
- Graham A. W., Driver S. P., 2005, *Pub. Astr. Soc. Australia*, 22, 118
- Graham A. W., Driver S. P., 2007, *ApJ*, 655, 77
- Graham A. W., Erwin P., Caon N., Trujillo I., 2001, *ApJ*, 563, L11
- Graham A. W., Erwin P., Caon N., Trujillo I., 2003, *Rev. Mex. Astron. Astrof. Conf. Ser.*, 17, 196
- Graham A. W., Li L., 2009, *ApJ*, 698, 812
- Granato G. L., De Zotti G., Silva L., Bressan A., Danese L., 2004, *ApJ*, 600, 580
- Greene J. E., Ho L. C., 2005, *ApJ*, 627, 721
- Gültekin K., et al. 2009, *ApJ*, 698, 198 (G09)
- Haehnelt M. G., Natarajan P., Rees M. J., 1998, *MNRAS*, 300, 817
- Häring N., Rix H., 2004, *ApJ*, 604, L89
- Ho L. C., 2007, *ApJ*, 668, 94
- Ho L. C., 2008, *ARA&A*, 46, 475
- Ho L. C., Darling J., Greene J. E., 2008a, *ApJS*, 177, 103
- Ho L. C., Darling J., Greene J. E., 2008b, *ApJ*, 681, 128
- Ho L. C., Filippenko A. V., Sargent W. L. W., 1997, *ApJS*, 112, 315
- Ho L. C., Greene J. E., Filippenko A. V., Sargent W. L. W., 2009, *ApJS*, 183, 1
- Hopkins P. F., Hernquist L., Cox T. J., Di Matteo T., Robertson B., Springel V., 2005a, *ApJ*, 630, 716
- Hopkins P. F., Hernquist L., Cox T. J., Di Matteo T., Martini P., Robertson B., Springel V., 2005b, *ApJ*, 630, 705
- Hopkins P. F., Hernquist L., Cox T. J., Di Matteo T., Robertson B., Springel V., 2006, *ApJS*, 163, 1
- Hopkins P. F., Hernquist L., Cox T. J., Robertson B., Krause E., 2007a, *ApJ*, 669, 45

- Hopkins P. F., Hernquist L., Cox T. J., Robertson B., Krause E., 2007b, *ApJ*, 669, 67
- Hopkins P. F., Murray N., Thompson T. A., 2009, *MNRAS*, 398, 303
- Hota A., Lim J., Ohyama Y., Saikia D. J., Dihn-v-Trung Croston J. H., 2009, in Saikia D. J., Green D. A., Gupta Y., Venturi T., eds., *ASP Conf. Ser. Vol. 407, The Low-Frequency Radio Universe*. Astron. Soc. Pac., San Francisco, p. 104
- Hu J., 2008, *MNRAS*, 386, 2242
- Hu J., 2009, submitted (arXiv/astro-ph:0908.2028)
- Isobe T., Feigelson E. D., Nelson P. I., 1986, *ApJ*, 306, 490
- Jørgensen I., Franx M., Kjaergaard P., 1995, *MNRAS*, 276, 1341
- Jørgensen I., Chiboucas K., Flint K., Bergmann M., Barr J., Davies R., 2007, *ApJ*, 654, L179
- Kaspi S., Smith P. S., Netzer H., Maoz D., Jannuzi B. T., Giveon U., 2000, *ApJ*, 533, 631
- Kormendy J., 2001, in Funes J. G., Corsini E. M., eds, *ASP Conf. Ser. 230, Galaxy Disks and Disk Galaxies*. Astron. Soc. Pac., San Francisco, p. 247
- Kormendy J., Kennicutt R. C. Jr., 2004, *ARA&A*, 42, 603
- Kormendy J., Bender R., 2009, *ApJ*, 691, L142
- Kormendy J., Bender R., 2011, *Nature*, 469, 377
- Kormendy J., Bender R., Cornell M. E., 2011, *Nature*, 469, 374
- Kormendy J., Fisher D. B., Cornell M. E., Bender R., 2009, *ApJS*, 182, 216
- Kormendy J., Gebhardt K., 2001, in Martel H., Wheeler J. C., eds, *The 20th Texas Symposium on Relativistic Astrophysics*. Am. Inst. Phys., New York, 586, 363
- Kormendy J., Richstone D., 1995, *ARA&A*, 33, 581
- Kronawitter A., Saglia R. P., Gerhard O., Bender R., 2000, *A&AS*, 144, 53
- Lauer T. R., et al. 2007, *ApJ*, 662, 808
- Lavalley M. P., Isobe T., Feigelson E. D., 1992, *BAAS*, 24, 839
- MacArthur L. A., Courteau S., Holtzman J. A., 2003, *ApJ*, 582, 689
- Magorrian J., et al. 1998, *AJ*, 115, 2285
- Marconi A., Hunt L. K., 2003, *ApJ*, 589, L21
- Markwardt C. B., 2009, in Bohlender D. A., Durand, D., P. Dowler, eds., *ASP Conf. Ser. Vol. 411, Astronomical Data Analysis Software and Systems XVIII*. Astron. Soc. Pac., San Francisco, p. 251
- McDonald M., Courteau S., Tully R. B., 2009, *MNRAS*, 394, 2022
- McDonald M., Courteau S., Tully R. B., Roediger J., 2011, *MNRAS*, 519
- McLure R. J., Dunlop J. S., 2002, *MNRAS*, 331, 795
- Méndez-Abreu J., 2008, PhD thesis, Università di Padova, Universidad de La Laguna
- Méndez-Abreu J., Aguerri J. A. L., Corsini E. M., Simonneau E., 2008, *A&A*, 478, 353
- Moffat A. F. J., 1969, *A&A*, 3, 455
- Monaco P., Fontanot F., Taffoni G., 2007, *MNRAS*, 375, 1189
- Moré J. J., Garbow B. S., Hillstrom K. E., 1980, User guide for MINPACK-1, Technical Report ANL-80-74. Argonne National Laboratory, Argonne
- Morse J. A., Cecil G., Wilson A. S., Tsvetanov Z. I., 1998, *ApJ*, 505, 159
- Novak G. S., Faber S. M., Dekel A., 2006, *ApJ*, 637, 96
- Oemler Jr. A., 1976, *ApJ*, 209, 693
- Patrel G., et al. 1997, *A&AS*, 124, 109
- Patrel G., Petit C., Prugniel P., Theureau G., Rousseau J., Brouty M., Dubois P., Cambrésy L., 2003, *A&A*, 412, 45
- Peng C. Y., 2010, in Peterson B., Somerville R., Storchi-Bergmann T., eds, *IAU Symp. 267 Co-Evolution of Central Black Holes and Galaxies*. Cambridge Univ. Press, Cambridge, p. 161
- Peterson B. M., Bentz M. C., 2006, *New Astr. Rev.*, 50, 796
- Pizzella A., Corsini E. M., Dalla Bontà E., Sarzi M., Coccato L., Bertola F., 2005, *ApJ*, 631, 785
- Quillen A. C., Frogel J. A., Gonzalez R. A., 1994, *ApJ*, 437, 162
- Robertson B., Cox T. J., Hernquist L., Franx M., Hopkins P. F., Martini P., Springel V., 2006a, *ApJ*, 641, 21
- Robertson B., Hernquist L., Cox T. J., Di Matteo T., Hopkins P. F., Martini P., Springel V., 2006b, *ApJ*, 641, 90
- Samurović S., Danziger I. J., 2005, *MNRAS*, 363, 769
- Sani, E., Marconi, A., Hunt, L. K., & Risaliti, G. 2011, *MNRAS*, 413, 1479
- Sarzi M., et al. 2002, *ApJ*, 567, 237
- Schawinski K., et al. 2006, *Nature*, 442, 888
- Schlegel D. J., Finkbeiner D. P., Davis M., 1998, *ApJ*, 500, 525
- Sérsic J. L., 1968, *Atlas de galaxias australes*. Observatorio Astronomico, Cordoba
- Shao Z., Xiao Q., Shen S., Mo H. J., Xia X., Deng Z., 2007, *ApJ*, 659, 1159
- Shields J. C., Walcher C. J., Böker T., Ho L. C., Rix H., van der Marel R. P., 2008, *ApJ*, 682, 104
- Sil'chenko O. K., Afanasiev V. L., 2004, *AJ*, 127, 2641
- Silk J., Rees M. J., 1998, *A&A*, 331, L1
- Somerville R. S., 2009, *MNRAS*, 399, 1988
- Springel V., Di Matteo T., Hernquist L., 2005, *MNRAS*, 361, 776
- Thomas, J., et al. 2011, *MNRAS*, 415, 545
- Tonry J. L., Dressler A., Blakeslee J. P., Ajhar E. A., Fletcher A. B., Luppino G. A., Metzger M. R., Moore C. B., 2001, *ApJ*, 546, 681
- Tremaine S., et al. 2002, *ApJ*, 574, 740
- Trujillo I., Erwin P., Asensio Ramos A., Graham A. W., 2004, *AJ*, 127, 1917
- Tully R. B., 1988, *Nearby Galaxies Catalog*. Cambridge Univ. Press, Cambridge
- Verheijen M. A. W., Sancisi R., 2001, *A&A*, 370, 765
- Vittorini V., Shankar F., Cavaliere A., 2005, *MNRAS*, 363, 1376
- Volonteri M., Haardt F., Madau P., 2003, *ApJ*, 582, 559
- Volonteri M., Natarajan P., 2009, *MNRAS*, 400, 1911
- Volonteri M., Natarajan P., Gültekin K., 2011, *ApJ*, 737, 50
- Wegner G., et al. 2003, *AJ*, 126, 2268
- Whitmore B. C., Schechter P. L., Kirshner R. P., 1979, *ApJ*, 234, 68
- Wyithe J. S. B., 2006, *MNRAS*, 365, 1082
- Williams M. J., Bureau M., Cappellari M., 2010, *MNRAS*, 409, 1330
- Wolf J., Martinez G. D., Bullock J. S., Kaplinghat M., Geha M., Muñoz R. R., Simon J. D., Avedo F. F., 2010,

MNRAS, 406, 1220

York, D. G., et al. 2000, AJ, 120, 1579

Young L. M., Bureau M., Cappellari M., 2008, ApJ, 676,
317

Younger J. D., Hopkins P. F., Cox T. J., Hernquist L.,
2008, ApJ, 686, 815

Zasov A. V., Petrochenko L. N., Cherepashchuk A. M.,
2005, Astronomy Reports, 49, 362

Table 1: Properties of the galaxies of the Sample A

Galaxy	Morph. T.	Spec. Cl.	D (Mpc)	Ref.	M_B^0 (mag)	σ_e (km s $^{-1}$)	i ($^\circ$)	Ref	V_C (km s $^{-1}$)	Ref	M_\bullet (33 $^\circ$) (M_\odot)	M_\bullet (81 $^\circ$) (M_\odot)	M_\bullet (M_\odot)
(1)	(2)	(3)	(4)	(5)	(6)	(7)	(8)	(9)	(10)	(11)	(12)	(13)	(14)
Upper limits on M_\bullet from B09													
IC 342	SABcd(rs)	H	3.73	1	-21.97	65.1 \pm 23.8	12	2	185.0 \pm 8.9	6	5.0E6	1.3E6	...
IC 3639	SBbc(rs):	S2*	44.80	2	-20.70	91.4 \pm 4.8	18	2	248.0 \pm 11.6	7	2.3E7	4.5E6	...
NGC 193	SAB0 $^-$ (s):	...	49.65	2	-20.22	185.0 \pm 17.1	40	2	5.2E8	1.2E8	...
NGC 289	SBbc(rs)	...	17.08	2	-19.91	108.9 \pm 11.6	47	2	240.1 \pm 1.8	7	4.7E7	1.2E7	...
NGC 315	E $^+$:	L1.9	57.68	2	-22.09	313.4 \pm 27.2	569 \pm 59*	8	1.7E9	4.0E8	...
NGC 383	SA0 $^-$:	...	59.17	2	-21.33	238.8 \pm 16.7	32	2	1.2E9	2.7E8	...
NGC 541	S0 $^-$:	...	63.65	2	-21.19	191.4 \pm 4.0	15	2	8.6E8	1.8E8	...
NGC 613	SBbc(rs)	H*	15.40	2	-20.56	125.3 \pm 18.9	42	2	240.1 \pm 3.9	9	9.0E7	1.8E7	...
NGC 741	E0:	...	65.71	2	-22.17	232.2 \pm 11.2	54	5	1.1E9	2.0E8	...
NGC 788	SA0/a(s)	S1/S2*	47.88	2	-20.75	127.3 \pm 18.2	45	2	1.6E8	4.4E7	...
NGC 1052	E4	L1.9	18.11	3	-20.09	191.4 \pm 6.2	82	2	189 \pm 18.9*	10	3.4E8	8.8E7	...
NGC 1358	SAB0/a(r)	S2	48.16	2	-20.86	171.5 \pm 18.5	41	2	180.4 \pm 14.3	7	4.9E8	1.1E8	...
NGC 1497	S0	...	75.32	2	-21.24	245.6 \pm 22.5	57	2	6.6E8	2.8E8	...
NGC 1667	SAB(r)c	S2	56.09	2	-21.49	178.0 \pm 28.9	40	2	236.6 \pm 13.1	9	2.7E8	9.3E7	...
NGC 1961	SABc(rs)	L2	48.63	2	-22.58	222.2 \pm 38.0	51	2	415.4 \pm 13.0	9	4.3E8	8.8E7	...
NGC 2110	SAB0 $^-$	S2*	29.12	2	-20.62	201.4 \pm 22.9	53	2	5.8E8	3.0E7	...
NGC 2179	SA0/a(s)	...	35.84	2	-20.09	154.3 \pm 11.2	51	2	251.7 \pm 17.4	9	3.5E8	1.2E8	...
NGC 2273	SBA(r):	S2	23.33	2	-19.97	116.7 \pm 10.6	44	2	223.3 \pm 6.5	9	6.6E6	2.0E6	...
NGC 2329	S0 $^-$:	...	72.33	2	-21.36	217.6 \pm 13.3	38	2	2.3E8	1.0E8	...
NGC 2685	(R)SB0 $^+$ pec	S2/T2:	12.51	2	-18.81	82.3 \pm 7.2	70	2	149.0 \pm 4.3	7	1.0E7	1.5E6	...
NGC 2892	E+ pec:	...	86.24	2	-20.78	297.1 \pm 18.8	22	5	3.5E8	2.1E8	...
NGC 2903	SABbc(rs)	H	10.45	2	-21.14	94.0 \pm 12.1	64	2	185.8 \pm 4.1	9	2.2E7	6.0E6	...
NGC 2911	SA0(s): pec	L2	43.49	2	-21.09	211.6 \pm 15.2	62	5	253.0 \pm 25.3	11	2.4E9	6.2E8	...
NGC 2964	SABbc(r):	H	19.69	2	-20.03	95.4 \pm 18.7	43	5	182.4 \pm 5.0	7	2.2E7	1.3E6	...
NGC 3021	SAbc(rs)	...	22.40	2	-19.37	56.4 \pm 24.8	58	2	127.4 \pm 4.1	9	3.7E7	9.1E6	...
NGC 3078	E2-3	...	32.85	3	-20.79	207.8 \pm 12.2	50	2	2.1E8	3.1E7	...
NGC 3081	(R)SAB0/a(r)	S2*	33.51	2	-20.19	123.0 \pm 7.6	43	2	136.9 \pm 5.1	7	3.2E7	7.9E6	...
NGC 3351	SBb(r)	H	9.33	4	-19.74	95.4 \pm 15.1	50	2	149.7 \pm 5.2	9	6.0E6	1.8E6	...
NGC 3368	SABab(rs)	L2	9.71	3	-20.28	105.3 \pm 4.1	49	2	205.2 \pm 5.8	9	4.5E7	1.4E7	...
NGC 3393	(R $^+$)SBA(rs):	S2*	50.59	2	-21.03	167.5 \pm 25.6	26	2	191.4 \pm 14.4	7	2.3E8	8.8E7	...
NGC 3627	SABb(s):	T2/S2	9.43	4	-20.88	97.2 \pm 7.5	68	5	168.4 \pm 4.1	9	1.4E7	6.3E6	...
NGC 3642	SAbc(r):	L1.9	21.65	2	-20.37	96.1 \pm 24.8	35	2	2.9E7	2.4E7	...
NGC 3675	SAb(s)	T2	12.41	2	-20.10	105.3 \pm 4.4	66	5	201.8 \pm 5.1	9	3.6E7	9.3E6	...
NGC 3801	S0?	...	46.29	2	-20.69	210.1 \pm 17.7	65	2	280.0 \pm 28	12	3.9E8	9.3E7	...
NGC 3862	E	...	84.56	2	-21.27	210.4 \pm 13.0	2	5	6.0E8	1.1E8	...
NGC 3953	SBbc(r)	T2	15.40	2	-20.71	128.5 \pm 0.9	63	2	207.5 \pm 4.3	9	4.2E7	1.1E7	...
NGC 3982	SABb(r):	S1.9	15.87	2	-19.47	78.0 \pm 2.0	31	5	161.5 \pm 6.8	9	1.6E7	4.9E6	...
NGC 3992	SBbc(rs)	T2:	15.31	2	-20.81	124.4 \pm 17.8	60	5	245.9 \pm 4.2	7	6.3E7	1.7E7	...
NGC 4036	S0 $^-$	L1.9	19.04	2	-20.06	163.8 \pm 5.4	87	5	1.8E8	3.4E7	...
NGC 4088	SABbc(rs)	H	11.85	2	-20.00	85.7 \pm 3.8	71	2	162.0 \pm 3.0	9	1.2E7	3.2E6	...
NGC 4143	SAB0 0 (s)	L1.9	14.84	3	-19.11	201.2 \pm 5.7	67	5	1.9E8	3.7E7	...
NGC 4150	SA0 0 (r)?	T2	12.79	3	-18.29	85.7 \pm 3.0	60	5	2.4E6	3.2E5	...
NGC 4203	SAB0 $^-$:	L1.9	14.09	3	-19.29	156.5 \pm 2.8	30	5	204.4 \pm 6.8	7	1.2E8	3.6E7	...
NGC 4212	SAc:	H	3.17	2	-16.28	67.8 \pm 2.8	54	2	133.6 \pm 5.0	7	2.6E6	3.7E5	...
NGC 4245	SB0/a(r):	H	14.56	2	-18.96	83.1 \pm 2.9	55	5	112.1 \pm 5.4	7	4.7E7	5.2E6	...
NGC 4278	E1-2	L1.9	15.03	3	-20.06	232.5 \pm 7.1	416 \pm 13*	8	1.7E8	4.9E7	...
NGC 4314	SBA(rs)	L2	15.49	2	-19.93	106.6 \pm 3.6	43	5	175 \pm 17.5*	13	1.6E7	4.1E6	...
NGC 4321	SABbc(s)	T2	14.19	4	-20.93	83.0 \pm 3.6	33	2	211.8 \pm 4.0	9	6.9E6	3.2E6	...
NGC 4335	E	...	59.08	2	-20.67	259.2 \pm 5.0	61	5	5.1E8	1.2E8	...
NGC 4429	SA0 $^+$ (r)	T2	18.20	2	-20.48	169.8 \pm 7.0	82	5	1.6E8	3.2E7	...
NGC 4450	SAab(s)	L1.9	28.28	2	-21.66	108.2 \pm 14.9	62	5	153.3 \pm 4.9	9	2.2E8	6.1E7	...
NGC 4477	SB0(s):?	S2	20.81	2	-20.44	144.8 \pm 8.9	37	5	7.1E7	1.8E7	...
NGC 4501	SAb(rs)	S2	32.29	2	-22.84	140.2 \pm 15.8	61	2	277.5 \pm 5.1	9	7.5E7	1.4E7	...
NGC 4507	(R $^+$)SABb(rs)	S2*	47.04	2	-21.23	143.9 \pm 6.9	39	2	3.4E7	6.8E6	...
NGC 4526	SAB0(s):	H	15.77	3	-20.61	195.4 \pm 2.7	83	5	357 \pm 17.85	14	3.0E8	5.7E7	...
NGC 4548	SBb(rs)	L2	17.92	3	-20.63	143.7 \pm 13.0	38	5	176.9 \pm 5.8	9	3.5E7	9.0E6	...
NGC 4552	E0-1	T2:	14.37	3	-20.36	233.5 \pm 10.5	28	5	1.8E9	6.4E8	...
NGC 4579	SABb(rs)	S1.9/L	22.96	2	-21.66	109.4 \pm 14.6	48	5	211.5 \pm 8.5	9	2.1E8	4.0E7	...
NGC 4636	E0-1	L1.9	13.72	3	-20.40	174.3 \pm 8.7	341 \pm 13*	8	6.3E8	2.3E8	...
NGC 4698	SAab(s)	S2	16.43	2	-19.99	123.9 \pm 8.3	62	5	256.1 \pm 3.9	9	8.3E7	4.0E7	...
NGC 4736	(R)SAab(r)	L2	4.85	3	-19.83	97.9 \pm 2.6	38	2	150.7 \pm 4.7	9	1.3E7	3.1E6	...
NGC 4800	SAb(rs)	H	12.51	2	-18.51	102.2 \pm 1.8	44	2	238.5 \pm 22.9	9	3.6E7	3.1E6	...
NGC 4826	(R)SAab(rs)	T2	7.00	3	-20.55	105.7 \pm 12.2	62	2	145.9 \pm 4.5	9	3.9E7	1.7E7	...
NGC 5005	SABbc(rs)	L1.9	14.65	2	-20.79	198.2 \pm 7.0	72	5	257.9 \pm 7.3	7	3.2E8	1.1E8	...
NGC 5127	E pec	...	62.53	2	-21.32	199.4 \pm 48.6	61	5	4.8E8	7.2E7	...
NGC 5194	SAbc(s) pec	S2	7.93	2	-20.99	70.3 \pm 9.4	54	2	83.5 \pm 2.2	9	2.1E6	4.0E5	...
NGC 5248	SABbc(rs)	H	17.92	2	-20.78	126.5 \pm 11.2	57	5	137.5 \pm 2.2	7	4.8E6	8.4E5	...
NGC 5252	S0	S1.9*	89.32	2	-20.97	168.8 \pm 24.0	87	5	120 \pm 12	15	6.5E8	1.2E8	...
NGC 5283	S0?	S2*	34.53	2	-18.72	136.1 \pm 12.9	28	2	5.5E7	1.2E7	...
NGC 5347	(R $^+$)SBab(rs)	S2*	32.29	2	-19.59	64.9 \pm 12.4	39	2	4.3E7	6.1E6	...
NGC 5427	SAC(s)pec	S2*	36.31	2	-21.22	64.8 \pm 11.4	32	2	230.1 \pm 30.7	7	7.6E7	1.9E7	...

Table 1 – Continued

Galaxy	Morph. T.	Spec. Cl.	D	Ref.	M_B^0	σ_e	i	Ref.	V_C	Ref.	M_\bullet (33 $^\circ$)	M_\bullet (81 $^\circ$)	M_\bullet
(1)	(2)	(3)	(Mpc)	(5)	(mag)	(km s $^{-1}$)	($^\circ$)	(9)	(km s $^{-1}$)	(11)	(M_\odot)	(M_\odot)	(M_\odot)
			(4)		(6)	(7)	(8)		(10)	(11)	(12)	(13)	(14)
NGC 5490	E	...	65.24	2	-21.34	260.6 \pm 24.9	59	5	1.2E9	2.4E8	...
NGC 5643	SABc(rs)	S2*	17.36	2	-21.11	89.5 \pm 1.0	30	2	155.1 \pm 3.9	7	4.4E7	2.9E6	...
NGC 5695	S?	S2*	54.60	2	-20.46	143.1 \pm 1.9	55	5	203.0 \pm 18.0	9	2.1E8	4.8E7	...
NGC 5728	SABa(r):	S2*	37.61	2	-21.37	193.4 \pm 40.4	60	2	205.3 \pm 7.5	9	2.2E8	5.8E7	...
NGC 5879	SABc(rs):?	T2/L2	10.55	2	-18.88	54.3 \pm 8.0	76	2	117.8 \pm 2.8	9	7.9E6	2.2E6	...
NGC 5921	SB(r)bc	L	20.49	2	-20.22	84.9 \pm 9.3	37	2	112.3 \pm 2.9	7	3.1E7	4.4E6	...
NGC 6300	SBb(rs)	S2*	14.19	2	-20.71	86.5 \pm 4.7	51	2	165.9 \pm 2.0	7	2.2E7	8.8E6	...
NGC 6500	SAab:	L2	36.49	2	-20.50	211.5 \pm 5.9	45	2	341.7 \pm 16.0	9	4.0E8	1.2E8	...
NGC 6861	SA0 $^-$ (s):	...	26.13	3	-20.32	404.2 \pm 36.2	65	2	1.4E9	3.4E8	...
NGC 6951	SABbc(rs)	S2	15.96	2	-20.45	95.5 \pm 9.8	35	2	241.3 \pm 5.4	9	1.3E7	5.5E6	...
NGC 7331	SAb(s)	T2	12.23	3	-21.21	115.8 \pm 4.1	75	2	244.6 \pm 4.1	9	1.6E8	6.9E7	...
NGC 7626	E pec:	L2::	38.08	2	-20.99	232.5 \pm 10.6	37	5	401 \pm 32*	8	8.1E8	1.8E8	...
NGC 7682	SBab(r)	S2*	59.27	2	-20.34	112.8 \pm 15.6	28	2	169.3 \pm 5.5	7	7.7E7	1.7E7	...
UGC 1214	(R)SAB0 $^+$ (rs):	S2*	59.92	2	-20.47	106.8 \pm 13.9	14	2	225.0 \pm 23.4	7	8.3E7	3.6E7	...
UGC 1395	SAb(rs)	S1.9*	60.85	2	-20.21	64.2 \pm 5.8	39	2	147.4 \pm 9.1	7	1.3E7	3.5E6	...
UGC 1841	E	...	74.95	2	-21.28	295.1 \pm 24.6	5	2	4.6E8	1.9E8	...
UGC 7115	E	...	88.20	2	-20.70	183.0 \pm 34.3	32	2	2.8E9	3.6E8	...
UGC 12064	S0 $^-$:	...	60.11	2	-20.19	258.7 \pm 17.6	5	2	2.3E9	2.1E8	...
Upper limits on M_\bullet from G09													
Abell 2052	E	...	151.1	G09	-22.14	233 \pm 11	71	2	4.9E9
NGC 3310	SB(r)bc	H	17.4	G09	-20.25	83 \pm 4	40	2	158.2 \pm 3.8	7	4.2E7
NGC 4041	S(rs)bc	H	20.9	G09	-19.84	88 \pm 4	28	2	255.3 \pm 3.8	7	6.4E6
NGC 4435	SB0	T2/H:	17.0	G09	-19.54	150 \pm 7	51	2	207.7 \pm 17.9	9	8.0E6
NGC 4486B	E1	...	17.0	G09	-16.91	185 \pm 9	56	2	248.7 \pm 17*	8	1.1E9

NOTES. — Col.(1): Galaxy name. Col.(2): Morphological type from RC3. Col.(3): Nuclear spectral class from Ho et al. (1997), where H = H II nucleus, L = LINER, S = Seyfert, T = transition object (LINER/H II), 1 = Seyfert 1, 2 = Seyfert 2, and a fractional number between 1 and 2 denotes various intermediate types; uncertain and highly uncertain classifications are followed by a single and double colon, respectively. The nuclear spectral class of galaxies marked with * is from the NASA/IPAC Extragalactic Database (NED). Col.(4): distance. All the distances were taken from the literature except those we obtained from V_{3K} the weighted mean recessional velocity corrected to the reference frame of the microwave background radiation given in RC3. These were derived as $D = V_{3K}/H_0$ with $H_0 = 70 \text{ km s}^{-1} \text{ Mpc}^{-1}$. For M_\bullet upper limits of G09 we adopted the distances from their paper. Col.(5): References for Col.(4). Col.(6): Absolute corrected B magnitude derived from B_T^0 (RC3) with the adopted distance. Col.(7): Central σ of the stellar component within r_e derived from the measured values taken from the same sources as B09 and corrected following Jørgensen et al. (1995). The value of UGC 1841 reported by B09 has been corrected adopting the effective radius by Donzelli et al. (2007). Col.(8): Inclination of the disc galaxies derived from either the fitted disc axial ratio (from this paper) or the isophotal axial ratio at a surface brightness of $\mu_B = 25 \text{ mag arcsec}^{-2}$ (from RC3) and the intrinsic disc axial ratio (derived following Paturel et al. (1997)). Col.(9): References for the apparent axial ratio adopted to calculate the inclination given in Col.(8). Col.(10): Circular velocity. The circular velocities were derived from either H I line-width measurements or gas resolved kinematics available in literature corrected according to the adopted inclination. Only the values marked with * are from dynamical models of the stellar component. Col.(11): References for Col.(10). Col.(12): M_\bullet upper limit of B09 for a Keplerian disc model assuming $i = 33^\circ$ and adopted distance. Col.(13): M_\bullet upper limit of B09 for $i = 81^\circ$ and adopted distance. Col.(14): M_\bullet upper limit of G09 and adopted distance.

REFERENCES. — (1) Tully (1988), (2) RC3, (3) Tonry et al. (2001), (4) Freedman et al. (2001), (5) this paper, (6) Pizzella et al. (2005), (7) HyperLeda, (8) Kronawitter et al. (2000), (9) Ho (2007), (10) Binney et al. (1990), (11) Sil'chenko & Afanasiev (2004), (12) Hota et al. (2009), (13) Quillen et al. (1994), (14) Young et al. (2008), (15) Morse et al. (1998).

Table 2: Properties of the galaxies of Sample B

Galaxy	Morph. T.	Spec. Cl.	D	$M_{V,T}^0$	$M_{V,bulge}^0$	σ_e	i	Ref.	V_c	Ref.	M_\bullet (low,high)
(1)	(2)	(3)	(Mpc)	(mag)	(mag)	(km s ⁻¹)	(°)	(9)	(km s ⁻¹)	(11)	(M _⊙)
(1)	(2)	(3)	(4)	(5)	(6)	(7)	(8)	(9)	(10)	(11)	(12)
Abell 1836-BCG	E	...	157.5	-23.31	-23.31 ± 0.15	288 ± 14	3.9E9(3.3,4.3)
Abell 3565-BCG	E	...	54.4	-23.27	-23.27 ± 0.15	322 ± 16	5.2E8(4.4,6.0)
Circinus	Sb	S2*	4.0	-17.36	...	158 ± 18	69	1	115.0 ± 5.9	3	1.7E6(1.4,2.1)
IC 1459	E4	L*	30.9	-22.57	-22.57 ± 0.15	340 ± 17	71	1	278 ± 27.8*	4	2.8E9(1.6,3.9)
MW	Sbc	...	0.008	105 ± 20	180.0 ± 20.0	5	4.1E6(3.5,4.7)
NGC 221	E2	...	0.86	-16.83	-16.83 ± 0.05	75 ± 3	57	2	3.1E6(2.5,3.7)
NGC 224	Sb	L	0.80	-21.84	...	160 ± 8	78	1	244.2 ± 6.0	3	1.5E8(1.2,2.4)
NGC 821	E4	...	25.5	-21.24	-21.24 ± 0.13	209 ± 10	73	2	4.2E7(3.4,7.0)
NGC 1023	SB0	...	12.1	-21.26	-20.61 ± 0.28	205 ± 10	88	1	270 ± 31*	6	4.6E7(4.1,5.1)
NGC 1068	Sb	S1.8	15.4	-22.17	...	151 ± 7	10	2	219.2 ± 5.0	3	8.6E6(8.3,8.9)
NGC 1390	Sb	...	20.2	-21.34	...	218 ± 10	50	1	153.7 ± 1.8	3	7.1E7(3.6,14)
NGC 1399	SBbc	...	20.1	-21.34	...	218 ± 10	50	1
NGC 1399	E1	...	21.1	-22.13	-22.13 ± 0.10	337 ± 16	424 ± 46*	7	1.3E9(0.6,1.8)
NGC 2748	Sb	H	24.9	-20.97	...	115 ± 5	72	1	128.4 ± 3.8	8	4.7E7(0.9,8.5)
NGC 2778	E2	...	24.2	-19.62	-19.62 ± 0.13	175 ± 8	1.6E7(0.6,2.5)
NGC 2787	SB0	L1.9	7.9	-18.90	...	189 ± 9	57	1	191.2 ± 20.5	3	4.3E7(3.8,4.7)
NGC 3031	Sb	S1.5	4.1	-21.51	...	143 ± 7	65	2	215.9 ± 7.0	3	8.0E7(6.9,10.0)
NGC 3115	S0	...	10.2	-21.25	-21.18 ± 0.05	230 ± 11	88	1	315 ± 10 *	9	9.6E8(6.7,15)
NGC 3227	SBa	S1.5	17.0	-20.73	...	133 ± 12	51	1	125.9 ± 4.8	8	1.5E7(0.7,2)
NGC 3245	S0	T2:	22.1	-20.96	...	205 ± 10	2.2E8(1.7,2.7)
NGC 3377	E6	...	11.7	-20.11	-20.11 ± 0.10	145 ± 7	1.1E8(1.0,2.2)
NGC 3379	E0	L2/T2::	11.7	-21.10	-21.10 ± 0.03	206 ± 10	259 ± 23*	7	1.2E8(0.6,2)
NGC 3384	SB0	...	11.7	-20.50	-19.93 ± 0.22	143 ± 7	77	2	1.8E7(1.5,1.9)
NGC 3585	S0	...	21.2	-21.88	-21.80 ± 0.20	213 ± 10	3.4E8(2.8,4.9)
NGC 3607	E1	L2	19.9	-21.62	-21.62 ± 0.10	229 ± 11	1.2E8(0.8,1.6)
NGC 3608	E1	L2/S2:	23.0	-21.05	-21.05 ± 0.10	182 ± 11	57	2	191 ± 43 *	10	2.1E8(1.4,3.2)
NGC 3998	S0	L1.9	14.9	-20.32	...	305 ± 15	46	1	462.3 ± 26.9	3	2.4E8(0.6,4.5)
NGC 4026	S0	...	15.6	-20.28	-19.83 ± 0.20	180 ± 9	2.1E8(1.7,2.8)
NGC 4258	SABbc	S1.9	7.2	-21.31	...	115 ± 10	71	1	202.4 ± 5.2	3	3.78E7(3.77,3.79)
NGC 4261	E2	L2	33.4	-22.72	-22.72 ± 0.06	315 ± 15	5.5E8(4.3,6.6)
NGC 4291	E2	...	25.0	-20.67	-20.67 ± 0.13	242 ± 12	3.2E8(0.8,4.1)
NGC 4342	S0	...	18.0	-18.84	...	225 ± 11	3.6E8(2.4,5.6)
NGC 4374	E1	L2	17.0	-22.45	-22.45 ± 0.05	296 ± 14	410 ± 31*	7	1.5E9(0.9,2.6)
NGC 4459	E2	H/L	17.0	-21.06	-21.06 ± 0.04	167 ± 8	7.4E7(6.0,8.8)
NGC 4473	E4	...	17.0	-21.14	-21.14 ± 0.04	190 ± 9	1.3E8(0.4,1.8)
NGC 4486	E1	L2	17.0	-22.92	-22.92 ± 0.04	375 ± 18	507 ± 38*	7	3.6E9(2.6,4.6)
NGC 4486A	E2	...	17.0	-18.70	-18.70 ± 0.05	111 ± 5	1.3E7(0.9,1.8)
NGC 4564	S0	...	17.0	-20.10	-19.60 ± 0.32	162 ± 8	6.9E7(5.9,7.3)
NGC 4594	Sa	L2	10.3	-22.52	-22.44 ± 0.15	240 ± 12	75	1	389.7 ± 9.4	3	5.7E8(1.7,11)
NGC 4596	SB0	L2::	18.0	-20.70	...	136 ± 6	54	2	154.9 ± 5.4	8	8.4E7(5.9,12)
NGC 4649	E2	...	16.5	-22.65	-22.65 ± 0.05	385 ± 19	2.1E9(1.5,2.6)
NGC 4697	E6	...	12.4	-21.29	-21.29 ± 0.11	177 ± 8	2.0E8(1.8,2.2)
NGC 5077	E3	L1.9	44.9	-22.04	-22.04 ± 0.13	222 ± 11	8.0E8(4.7,13)
NGC 5128	S0/E	S2	4.4	-21.82	-21.82 ± 0.08	150 ± 7	46	1	325.3 ± 16.7	8	7.0E7(3.2,8.3)
NGC 5576	E3	...	27.1	-21.26	-21.26 ± 0.13	183 ± 9	81	2	1.8E8(1.4,2.1)
NGC 5845	E3	...	28.7	-19.77	-19.77 ± 0.13	234 ± 11	2.9E8(1.2,3.4)
NGC 6251	E1	S2	106.0	290 ± 14	6.0E8(4.0,8.0)
NGC 7052	E3	...	70.9	266 ± 13	71	1	4.0E8(2.4,6.8)
NGC 7457	S0	...	14.0	-19.80	-18.72 ± 0.11	67 ± 3	4.1E6(2.4,5.3)
NGC 7582	SBab	S2	22.3	-21.51	...	156 ± 19	72	1	121.4 ± 3.2	8	5.5E7(4.4,7.1)

NOTES. — Col.(1): Galaxy name. Col.(2): Morphological type from G09. Col.(3): Nuclear spectral class from Ho et al. (1997), where H = H II nucleus, L = LINER, S = Seyfert, T = transition object (LINER/H II), 1 = Seyfert 1, 2 = Seyfert 2, and a fractional number between 1 and 2 denotes various intermediate types; uncertain and highly uncertain classifications are followed by a single and double colon, respectively. The nuclear spectral class of galaxies marked with * is from NED. Col.(4): Distance from G09. Col.(5): Absolute corrected total V magnitude from G09. Col.(6): Absolute corrected V magnitude of the bulge from G09. Col.(7): Central velocity dispersion of the stellar component within r_e from G09. Col.(8): Inclination of the disc galaxies derived from either the fitted disc axial ratio (from this paper) or the isophotal axial ratio at a surface brightness of $\mu_B = 25$ mag arcsec⁻² (from RC3) and the intrinsic disc axial ratio (derived following Paturel et al. (1997)). Col.(9): References for the apparent axial ratio adopted to calculate the inclination given in Col.(8). Col.(10): Circular velocity. The circular velocities were derived from either H I line-width measurements or gas resolved kinematics available in literature corrected according to the adopted inclination. Only the values marked with * are from dynamical models of the stellar component. Col.(11): References for Col.(10). Col.(12): Mass (and confidence interval) of the SMBH derived from modelling based on the resolved kinematics from G09. REFERENCES. — (1) RC3, (2) this paper, (3) Ho (2007), (4) Samurović & Danziger (2005), (5) Baes et al. (2003), (6) Debattista et al. (2002), (7) Kronawitter et al. (2000), (8) Paturel et al. (2003), (9) Bender et al. (1994), (10) Coccato et al. (2009).

Table 3: Structural parameters of the galaxies from the azimuthally-averaged light profiles measured in g and i -band SDSS images.

Galaxy	$m_{\text{tot},g}$ (mag)	$m_{\text{tot},i}$ (mag)	PA ($^{\circ}$)	ϵ	$m_{24.5}$ (mag)	$R_{24.5}$ ($''$)	$\mu_{e,\text{gal}}$ (mag arcsec $^{-2}$)	$r_{e,\text{gal}}$ ($''$)	C_{28}
(1)	(2)	(3)	(4)	(5)	(6)	(7)	(8)	(9)	(10)
Galaxies from Sample A: upper limit on M_{\bullet} from B09									
NGC 741	11.35 \pm 0.12	10.55 \pm 0.11	8.11	0.25	10.74	142.60	22.84	64.76	5.33
NGC 1052	10.80 \pm 0.11	9.65 \pm 0.10	141.62	0.19	9.71	151.82	19.87	28.98	4.77
NGC 1667	12.23 \pm 0.12	11.69 \pm 0.12	67.00	0.26	11.71	59.57	20.49	18.22	3.15
NGC 2685	11.15 \pm 0.11	10.22 \pm 0.10	3.71	0.52	10.30	141.32	20.21	31.26	5.10
NGC 2892	12.77 \pm 0.13	11.71 \pm 0.12	164.31	0.18	11.82	72.27	21.79	21.44	5.28
NGC 2903	8.92 \pm 0.09	8.08 \pm 0.08	54.50	0.46	8.10	308.12	20.17	94.85	1.89
NGC 2911	11.73 \pm 0.12	10.63 \pm 0.11	129.46	0.35	10.75	138.18	21.96	42.13	4.90
NGC 2964	11.30 \pm 0.11	10.50 \pm 0.11	162.05	0.48	10.53	102.10	20.01	31.16	2.94
NGC 3021	12.18 \pm 0.12	11.40 \pm 0.11	142.43	0.37	11.42	59.09	19.80	19.69	3.20
NGC 3351	10.06 \pm 0.10	9.03 \pm 0.09	64.60	0.10	9.06	199.27	20.79	62.43	4.16
NGC 3368	9.54 \pm 0.10	8.47 \pm 0.09	104.57	0.19	8.51	239.62	19.94	57.12	4.30
NGC 3627	8.76 \pm 0.09	7.98 \pm 0.08	93.08	0.52	8.01	359.49	20.21	79.79	3.56
NGC 3642	11.73 \pm 0.12	10.96 \pm 0.11	107.72	0.13	11.14	95.44	21.44	28.22	4.54
NGC 3675	10.06 \pm 0.10	8.97 \pm 0.09	79.91	0.39	9.04	239.51	20.45	73.02	3.54
NGC 3801	12.05 \pm 0.12	10.97 \pm 0.11	144.11	0.39	11.07	112.49	21.17	30.81	4.49
NGC 3862	12.17 \pm 0.13	11.14 \pm 0.11	121.80	0.34	11.40	116.84	22.73	42.87	5.94
NGC 3953	10.15 \pm 0.10	9.19 \pm 0.09	69.23	0.52	9.22	204.72	20.88	62.31	3.72
NGC 3982	11.75 \pm 0.12	11.05 \pm 0.11	89.38	0.13	11.07	65.24	19.93	18.09	2.33
NGC 3992	9.83 \pm 0.10	8.98 \pm 0.09	17.60	0.51	9.02	239.99	21.29	90.88	2.80
NGC 4036	10.74 \pm 0.11	9.69 \pm 0.10	4.46	0.51	9.72	140.08	19.33	29.33	4.43
NGC 4088	10.15 \pm 0.10	9.47 \pm 0.09	34.26	0.64	9.49	182.01	20.54	68.32	2.52
NGC 4143	11.33 \pm 0.11	10.21 \pm 0.10	121.10	0.32	10.23	88.69	19.17	17.19	4.64
NGC 4150	11.85 \pm 0.12	10.86 \pm 0.11	123.60	0.33	10.89	78.23	20.00	17.19	4.78
NGC 4203	10.93 \pm 0.11	9.77 \pm 0.10	82.54	0.09	9.80	122.53	20.43	29.20	4.89
NGC 4212	11.19 \pm 0.11	10.38 \pm 0.10	13.46	0.34	10.40	99.19	20.38	39.46	2.68
NGC 4245	11.55 \pm 0.12	10.47 \pm 0.11	97.00	0.20	10.52	112.39	20.71	33.72	4.38
NGC 4278	10.52 \pm 0.11	9.40 \pm 0.09	53.47	0.09	9.45	156.47	19.90	26.21	4.89
NGC 4314	10.81 \pm 0.11	9.70 \pm 0.10	178.77	0.12	9.75	152.44	20.55	59.58	4.32
NGC 4321	9.53 \pm 0.10	8.67 \pm 0.09	79.18	0.16	8.71	261.30	21.08	114.94	2.58
NGC 4335	12.32 \pm 0.13	11.27 \pm 0.11	120.07	0.22	11.37	83.81	20.75	17.63	5.32
NGC 4429	9.95 \pm 0.10	8.93 \pm 0.09	178.12	0.56	8.96	231.68	20.19	57.68	4.24
NGC 4450	10.13 \pm 0.10	9.13 \pm 0.09	93.86	0.43	9.17	218.24	20.74	58.04	4.08
NGC 4477	10.73 \pm 0.11	9.58 \pm 0.10	19.31	0.14	9.61	142.18	20.51	34.81	4.39
NGC 4501	9.81 \pm 0.10	9.05 \pm 0.09	131.35	0.48	9.07	236.04	20.60	73.04	3.23
NGC 4526	9.46 \pm 0.10	8.50 \pm 0.09	159.75	0.70	8.54	337.08	19.75	45.57	5.23
NGC 4548	10.32 \pm 0.10	9.20 \pm 0.09	123.32	0.20	9.28	217.25	21.52	80.08	3.82
NGC 4552	10.15 \pm 0.10	9.02 \pm 0.09	142.26	0.13	9.07	202.90	20.07	34.11	5.37
NGC 4579	9.64 \pm 0.10	8.61 \pm 0.09	177.58	0.25	8.68	251.94	20.76	77.27	4.23
NGC 4636	9.73 \pm 0.10	8.63 \pm 0.09	144.03	0.20	8.68	264.19	20.94	72.16	4.43
NGC 4698	10.94 \pm 0.11	9.84 \pm 0.10	111.10	0.11	9.89	134.68	20.31	35.10	4.47
NGC 4736	8.24 \pm 0.09	7.55 \pm 0.08	2.81	0.47	7.79	383.92	20.04	63.14	6.64
NGC 4800	11.68 \pm 0.12	10.70 \pm 0.11	71.94	0.07	10.73	75.43	19.81	20.53	3.63
NGC 4826	8.84 \pm 0.09	8.12 \pm 0.08	159.61	0.49	8.13	299.77	19.93	77.97	3.23
NGC 5005	9.74 \pm 0.10	8.78 \pm 0.09	32.04	0.53	8.81	207.82	19.73	51.96	3.97
NGC 5127	12.56 \pm 0.13	11.46 \pm 0.12	25.55	0.29	11.58	82.72	21.41	23.31	4.63
NGC 5194	8.67 \pm 0.09	8.11 \pm 0.08	84.80	0.36	8.12	328.36	20.91	115.51	3.18
NGC 5248	10.51 \pm 0.11	9.56 \pm 0.10	138.61	0.16	9.60	165.17	20.72	66.22	3.58
NGC 5252	12.83 \pm 0.13	11.93 \pm 0.12	83.50	0.45	12.04	68.31	20.83	17.92	4.64
NGC 5347	12.87 \pm 0.13	11.91 \pm 0.12	165.10	0.07	11.98	59.64	21.34	30.66	3.46
NGC 5490	12.27 \pm 0.12	11.15 \pm 0.11	92.15	0.22	11.23	84.70	20.67	16.69	5.50
NGC 5695	12.99 \pm 0.13	11.95 \pm 0.12	151.27	0.26	12.00	57.14	20.48	14.98	4.07
NGC 5879	11.30 \pm 0.11	10.62 \pm 0.11	122.79	0.61	10.67	125.47	20.36	26.91	4.09
NGC 5921	11.03 \pm 0.11	10.27 \pm 0.10	147.44	0.25	10.44	160.99	22.27	61.04	3.86
NGC 7331	9.61 \pm 0.10	8.75 \pm 0.09	161.29	0.58	8.80	285.70	20.30	67.00	4.47
NGC 7626	11.56 \pm 0.12	10.69 \pm 0.11	5.53	0.14	10.72	104.39	21.05	27.18	4.52
UGC 1395	13.66 \pm 0.14	13.01 \pm 0.13	112.82	0.08	13.05	38.71	21.56	18.01	3.15
UGC 7115	13.15 \pm 0.14	12.04 \pm 0.12	96.41	0.28	12.28	66.21	21.95	17.77	6.33
Galaxies from Sample A: upper limit on M_{\bullet} from G09									
Abell 2052	12.47 \pm 0.13	11.58 \pm 0.12	53.05	0.36	11.74	104.37	23.17	52.44	4.37
NGC 3310	10.83 \pm 0.11	10.48 \pm 0.11	78.70	0.04	10.56	107.72	19.66	16.30	4.16
NGC 4041	11.42 \pm 0.12	10.57 \pm 0.11	12.03	0.13	10.63	100.88	20.47	21.22	3.90
NGC 4435	11.01 \pm 0.11	9.93 \pm 0.10	76.36	0.24	9.95	111.64	19.48	23.96	4.73
NGC 4486B	13.74 \pm 0.14	12.75 \pm 0.13	175.94	0.29	12.79	28.21	18.17	2.99	4.47
Galaxies from Sample B									
Abell 1836	13.24 \pm 0.14	12.03 \pm 0.12	107.86	0.22	12.17	63.47	21.57	17.61	4.80
NGC 0821	11.10 \pm 0.11	10.33 \pm 0.10	169.09	0.28	10.39	139.90	21.15	35.01	5.03
NGC 1068	8.97 \pm 0.09	8.12 \pm 0.08	5.51	0.30	8.17	329.45	19.67	44.48	5.63
NGC 2778	12.85 \pm 0.13	11.74 \pm 0.12	13.21	0.19	11.77	53.45	20.19	12.02	4.57

Table 3 – Continued

Galaxy	$m_{\text{tot,g}}$	$m_{\text{tot,i}}$	PA	ϵ	$m_{24.5}$	$R_{24.5}$	$\mu_{\text{e,gal}}$	$r_{\text{e,gal}}$	C_{28}
(1)	(mag)	(mag)	($^{\circ}$)	(5)	(mag)	($''$)	(mag arcsec $^{-2}$)	($''$)	(10)
	(2)	(3)	(4)		(6)	(7)	(8)	(9)	
NGC 3031	7.76 ± 0.08	6.76 ± 0.07	86.85	0.42	6.79	396.00	19.40	94.61	4.09
NGC 3227	10.78 ± 0.11	9.84 ± 0.10	106.11	0.47	9.91	162.41	20.77	59.08	3.30
NGC 3245	11.03 ± 0.11	9.97 ± 0.10	78.83	0.38	10.05	127.01	19.95	26.68	5.15
NGC 3377	10.24 ± 0.11	9.34 ± 0.10	2.80	0.11	9.51	201.63	21.23	59.52	5.00
NGC 3379	9.67 ± 0.10	8.49 ± 0.09	4.39	0.11	8.54	246.37	20.00	56.99	5.26
NGC 3384	9.80 ± 0.10	8.85 ± 0.09	28.09	0.56	8.88	227.66	20.14	37.69	5.74
NGC 3607	10.32 ± 0.10	9.18 ± 0.09	136.66	0.10	9.24	183.12	20.22	36.42	4.79
NGC 3608	11.23 ± 0.11	10.13 ± 0.10	15.55	0.14	10.19	123.25	20.48	28.42	4.87
NGC 3998	10.81 ± 0.11	9.68 ± 0.10	129.80	0.19	9.73	128.72	19.67	20.40	5.47
NGC 4026	10.65 ± 0.11	9.69 ± 0.10	90.02	0.63	9.70	138.74	18.88	21.11	5.50
NGC 4258	8.63 ± 0.09	7.94 ± 0.08	118.60	0.45	7.97	517.97	20.97	135.85	4.13
NGC 4261	10.18 ± 0.11	9.15 ± 0.09	99.42	0.32	9.36	236.04	21.38	56.63	5.78
NGC 4342	12.51 ± 0.13	11.26 ± 0.11	102.67	0.26	11.34	57.41	18.06	7.59	5.91
NGC 4374	9.56 ± 0.10	8.37 ± 0.08	175.20	0.06	8.42	258.44	20.38	53.79	4.89
NGC 4459	10.45 ± 0.11	9.23 ± 0.09	176.05	0.25	9.34	200.03	20.66	40.99	5.24
NGC 4473	10.34 ± 0.10	9.27 ± 0.09	178.13	0.35	9.33	192.68	20.00	34.79	5.49
NGC 4486	9.21 ± 0.09	8.03 ± 0.08	139.27	0.16	8.06	301.70	20.20	68.38	4.46
NGC 4486A	11.11 ± 0.12	11.20 ± 0.11	170.01	0.34	11.04	111.52	18.32	5.82	4.44
NGC 4564	11.21 ± 0.11	10.15 ± 0.10	41.86	0.41	10.18	113.23	19.45	22.41	5.14
NGC 4596	10.63 ± 0.11	9.56 ± 0.10	161.17	0.24	9.61	164.73	20.73	56.20	4.50
NGC 4649	9.18 ± 0.09	7.96 ± 0.08	167.95	0.21	8.01	322.54	20.14	67.47	4.80
NGC 4697	9.64 ± 0.10	8.53 ± 0.09	119.54	0.25	8.57	253.13	20.24	59.72	4.36
NGC 5576	10.61 ± 0.11	9.52 ± 0.10	6.18	0.46	9.76	202.00	21.43	49.36	6.82
NGC 5845	12.64 ± 0.13	11.45 ± 0.11	140.39	0.22	11.48	50.59	17.68	4.34	4.91

NOTES. — Col.(1): Galaxy name. Col.(2): Total extrapolated g -band magnitude of the galaxy. Col.(3): Total extrapolated i -band magnitude of the galaxy. Col.(4): Position angle of the isophotes. Col.(5): Ellipticity of the isophotes. Col.(6): Integrated i -band magnitude within the isophote at a surface brightness level of 24.5 mag arcsec $^{-2}$ corrected for Galactic extinction, K-correction, and internal extinction following (Shao et al. 2007). Col.(7): Radius of isophote at a surface brightness level of $\mu_i = 24.5$ mag arcsec $^{-2}$. Col.(8): Effective surface brightness of the galaxy. Col.(9): Effective radius of the galaxy. Col.(10): Concentration index $C_{28} = 5 \log(r_{80}/r_{20})$ where r_{80} and r_{20} are the radii that enclose 80% and 20% of total light, respectively.

Table 4: Structural properties of the sample galaxies from two-dimensional decomposition of the i -band SDSS images

Galaxy	2D Fit	Comments	μ_e (mag arcsec $^{-2}$)	r_e ($''$)	n	q_b	PA $_b$ ($^\circ$)	μ_0 (mag arcsec $^{-2}$)	h ($''$)	q_d	PA $_d$ ($^\circ$)	B/T	$m_{i,bulge}$ (mag)
(1)	(2)	(3)	(4)	(5)	(6)	(7)	(8)	(9)	(10)	(11)	(12)	(13)	(14)
Galaxies from Sample A: upper limits on M_\bullet from B09													
NGC 741	yes	$r^{1/n}$	22.56 ± 0.07	61.75 ± 2.15	4.50 ± 0.09	0.81 ± 0.01	177.00 ± 0.02	1.00	10.38 ± 0.04
NGC 1052	no	bad
NGC 1667	no	bad
NGC 2685	no	bad
NGC 2892	yes	$r^{1/n}+exp.$	20.07 ± 0.34	7.04 ± 1.86	3.46 ± 0.41	0.97 ± 0.01	101.84 ± 25.04	20.81 ± 0.42	20.79 ± 9.29	0.95 ± 0.09	51.86 ± 0.55	0.44 ± 0.18	12.56 ± 0.28
NGC 2903	no	bad
NGC 2911	yes	$r^{1/n}+exp.$	20.82 ± 0.13	16.73 ± 1.44	3.66 ± 0.20	0.74 ± 0.01	56.01 ± 4.87	21.53 ± 0.21	60.99 ± 12.04	0.62 ± 0.02	48.66 ± 0.14	0.37 ± 0.05	11.69 ± 0.07
NGC 2964	yes	$r^{1/n}+exp.$	17.94 ± 0.39	1.44 ± 0.47	2.68 ± 0.34	0.85 ± 0.02	1.34 ± 0.14	18.86 ± 0.60	18.73 ± 14.78	0.75 ± 0.22	30.87 ± 1.42	0.04 ± 0.01	14.16 ± 0.61
NGC 3021	no	bar
NGC 3351	no	bar
NGC 3368	no	bar
NGC 3627	yes	$r^{1/n}+exp.$	21.30 ± 0.02	98.00 ± 0.96	4.56 ± 0.01	0.45 ± 0.01	69.30 ± 0.45	19.61 ± 0.02	78.64 ± 0.32	0.44 ± 0.01	100.77 ± 0.02	0.56 ± 0.01	7.40 ± 0.01
NGC 3642	no	embedded disc
NGC 3675	yes	$r^{1/n}+exp.$	20.96 ± 0.15	30.13 ± 3.90	4.73 ± 0.23	0.49 ± 0.01	100.94 ± 10.52	19.36 ± 0.29	48.77 ± 12.75	0.47 ± 0.02	98.86 ± 0.23	0.26 ± 0.03	10.85 ± 0.14
NGC 3801	no	bad
NGC 3862	yes	$r^{1/n}+exp.$	24.13 ± 0.16	75.40 ± 4.88	7.90 ± 0.30	1.00 ± 0.01	78.66 ± 0.02	1.00	10.99 ± 0.04
NGC 3953	no	bar
NGC 3982	yes	$r^{1/n}+exp.$	17.87 ± 0.39	1.58 ± 0.51	0.80 ± 0.10	0.79 ± 0.01	106.83 ± 11.36	18.38 ± 0.58	12.00 ± 9.47	0.87 ± 0.26	108.84 ± 5.00	0.04 ± 0.01	14.55 ± 0.62
NGC 3992	yes	$r^{1/n}+exp.$	21.44 ± 0.16	31.64 ± 4.10	5.33 ± 0.26	0.67 ± 0.01	149.86 ± 15.61	20.15 ± 0.30	80.39 ± 21.02	0.54 ± 0.02	155.01 ± 0.35	0.20 ± 0.02	10.83 ± 0.14
NGC 4036	yes	$r^{1/n}+exp.$	17.97 ± 0.12	4.05 ± 0.35	1.68 ± 0.09	0.88 ± 0.01	153.72 ± 13.35	17.83 ± 0.17	19.91 ± 3.93	0.48 ± 0.01	175.07 ± 0.50	0.17 ± 0.02	12.12 ± 0.08
NGC 4088	no	Freeman II disc
NGC 4143	yes	$r^{1/n}+exp.$	16.79 ± 0.11	3.07 ± 0.26	1.05 ± 0.06	0.78 ± 0.01	59.33 ± 5.15	17.84 ± 0.17	14.27 ± 2.82	0.58 ± 0.02	58.73 ± 0.17	0.24 ± 0.03	11.91 ± 0.08
NGC 4150	yes	$r^{1/n}+exp.$	17.27 ± 0.30	2.32 ± 0.61	1.68 ± 0.20	0.76 ± 0.01	53.89 ± 13.25	18.83 ± 0.38	14.58 ± 6.52	0.65 ± 0.06	57.08 ± 0.60	0.23 ± 0.09	12.80 ± 0.28
NGC 4203	yes	$r^{1/n}+exp.$	18.49 ± 0.13	7.99 ± 1.03	2.62 ± 0.13	0.87 ± 0.01	99.39 ± 10.35	19.92 ± 0.30	34.02 ± 8.89	0.91 ± 0.04	102.13 ± 0.23	0.37 ± 0.04	10.95 ± 0.14
NGC 4212	no	Freeman II disc
NGC 4245	yes	$r^{1/n}+exp.$	18.92 ± 0.12	5.79 ± 0.50	2.00 ± 0.11	0.83 ± 0.01	60.60 ± 5.26	19.49 ± 0.19	24.55 ± 4.84	0.64 ± 0.02	52.31 ± 0.15	0.24 ± 0.03	12.27 ± 0.08
NGC 4278	yes	$r^{1/n}$	20.11 ± 0.07	28.34 ± 0.99	3.70 ± 0.07	0.87 ± 0.01	107.34 ± 0.01	1.00	9.65 ± 0.03
NGC 4314	yes	$r^{1/n}+exp.$	19.10 ± 0.10	16.24 ± 1.09	2.90 ± 0.10	0.86 ± 0.01	105.17 ± 4.12	20.88 ± 0.12	48.11 ± 2.07	0.76 ± 0.01	170.28 ± 0.11	0.67 ± 0.03	9.99 ± 0.09
NGC 4321	no	bar
NGC 4335	yes	$r^{1/n}$	21.06 ± 0.14	19.34 ± 1.25	5.10 ± 0.19	0.77 ± 0.01	64.27 ± 0.02	1.00	11.40 ± 0.04
NGC 4429	yes	$r^{1/n}+exp.$	20.37 ± 0.10	29.74 ± 2.00	3.31 ± 0.11	0.65 ± 0.01	2.18 ± 0.09	19.31 ± 0.11	52.21 ± 2.25	0.44 ± 0.01	8.23 ± 0.01	0.44 ± 0.02	10.17 ± 0.09
NGC 4450	yes	$r^{1/n}+exp.$	20.27 ± 0.15	18.05 ± 2.34	3.98 ± 0.20	0.77 ± 0.01	92.95 ± 9.68	19.35 ± 0.29	41.51 ± 10.85	0.53 ± 0.02	90.80 ± 0.21	0.30 ± 0.03	10.89 ± 0.14
NGC 4477	yes	$r^{1/n}+exp.$	19.22 ± 0.14	14.52 ± 1.88	2.62 ± 0.13	0.75 ± 0.01	105.63 ± 11.00	20.22 ± 0.30	42.62 ± 11.14	0.85 ± 0.03	164.34 ± 0.37	0.43 ± 0.04	10.56 ± 0.14
NGC 4501	no	Freeman II disc
NGC 4526	yes	$r^{1/n}+exp.$	18.14 ± 0.09	11.92 ± 0.80	1.90 ± 0.06	0.68 ± 0.01	23.35 ± 0.91	19.00 ± 0.11	53.19 ± 2.29	0.43 ± 0.01	22.59 ± 0.01	0.37 ± 0.02	10.17 ± 0.09
NGC 4548	yes	$r^{1/n}+exp.$	21.08 ± 0.15	24.98 ± 3.23	4.47 ± 0.22	0.85 ± 0.01	174.33 ± 18.16	20.12 ± 0.30	51.94 ± 13.58	0.81 ± 0.03	167.78 ± 0.38	0.28 ± 0.03	10.83 ± 0.14
NGC 4552	yes	$r^{1/n}$	20.61 ± 0.07	45.24 ± 1.57	4.30 ± 0.08	0.94 ± 0.01	33.69 ± 0.01	1.00	8.98 ± 0.03
NGC 4579	yes	$r^{1/n}+exp.$	20.77 ± 0.10	39.13 ± 2.63	5.24 ± 0.18	0.70 ± 0.01	157.41 ± 6.16	19.76 ± 0.11	53.30 ± 2.30	0.69 ± 0.01	153.18 ± 0.10	0.47 ± 0.02	9.67 ± 0.08
NGC 4636	yes	$r^{1/n}+exp.$	19.49 ± 0.10	19.42 ± 1.30	2.18 ± 0.07	0.95 ± 0.01	149.80 ± 5.87	20.21 ± 0.11	83.59 ± 3.60	0.69 ± 0.01	142.29 ± 0.09	0.28 ± 0.01	10.03 ± 0.09
NGC 4698	yes	$r^{1/n}+exp.$	19.47 ± 0.14	10.47 ± 1.36	3.00 ± 0.15	0.90 ± 0.01	162.53 ± 16.93	19.39 ± 0.29	34.24 ± 8.95	0.53 ± 0.02	75.80 ± 0.17	0.32 ± 0.03	11.25 ± 0.15
NGC 4736	no	bar
NGC 4800	no	Freeman II disc
NGC 4826	yes	$r^{1/n}+exp.$	16.94 ± 0.12	5.01 ± 0.65	1.49 ± 0.07	0.65 ± 0.01	18.62 ± 1.94	17.97 ± 0.27	50.79 ± 13.28	0.60 ± 0.02	16.50 ± 0.04	0.06 ± 0.01	11.04 ± 0.15
NGC 5005	yes	$r^{1/n}+exp.$	18.95 ± 0.09	23.21 ± 1.56	2.04 ± 0.07	0.43 ± 0.01	153.25 ± 6.00	19.31 ± 0.11	58.58 ± 2.52	0.38 ± 0.01	147.97 ± 0.09	0.40 ± 0.02	10.00 ± 0.09
NGC 5127	yes	$r^{1/n}$	22.56 ± 0.15	39.95 ± 2.59	4.90 ± 0.19	0.77 ± 0.01	151.27 ± 0.04	1.00	11.34 ± 0.04
NGC 5194	no	bad
NGC 5248	yes	$r^{1/n}+exp.$	18.62 ± 0.12	7.05 ± 0.61	0.99 ± 0.05	0.69 ± 0.01	19.26 ± 1.67	19.53 ± 0.19	45.68 ± 9.02	0.58 ± 0.02	33.52 ± 0.10	0.11 ± 0.01	12.09 ± 0.08
NGC 5252	yes	$r^{1/n}+exp.$	20.56 ± 0.35	9.92 ± 2.62	4.82 ± 0.57	0.41 ± 0.01	102.66 ± 25.24	19.61 ± 0.39	11.57 ± 5.17	0.48 ± 0.05	100.86 ± 1.07	0.51 ± 0.21	13.06 ± 0.29
NGC 5347	no	Freeman II disc
NGC 5490	yes	$r^{1/n}$	22.13 ± 0.15	35.09 ± 2.27	6.90 ± 0.26	0.78 ± 0.01	82.69 ± 0.02	1.00	11.00 ± 0.04
NGC 5695	yes	$r^{1/n}+exp.$	18.50 ± 0.40	2.00 ± 0.65	3.75 ± 0.47	0.69 ± 0.01	14.84 ± 1.58	19.11 ± 0.61	10.79 ± 8.51	0.63 ± 0.19	27.16 ± 1.25	0.19 ± 0.05	14.04 ± 0.60
NGC 5879	no	bad
NGC 5921	no	bar
NGC 7331	no	bad
NGC 7626	yes	$r^{1/n}$	22.69 ± 0.08	67.08 ± 2.33	5.54 ± 0.11	0.90 ± 0.01	101.47 ± 0.01	1.00	10.11 ± 0.03
UGC 1395	no	bad
UGC 7115	yes	$r^{1/n}$	22.43 ± 0.34	22.01 ± 3.91	7.05 ± 0.52	0.92 ± 0.01	89.26 ± 0.06	1.00	12.12 ± 0.19
Galaxies from Sample A: upper limit on M_\bullet from G09													
Abell 2052	no	$r^{1/n}$	24.58 ± 0.17	127.48 ± 8.26	4.57 ± 0.17	0.72 ± 0.01	116.52 ± 0.03	1.00	10.94 ± 0.04
NGC 3310	no	bar
NGC 4041	yes	$r^{1/n}+exp.$	19.09 ± 0.14	$10.46 \pm$									

Table 4 – Continued

Galaxy	2D Fit	Comments	μ_e (mag arcsec ⁻²) (4)	r_e ($''$) (5)	n (6)	q_b (7)	PA_b ($^\circ$) (8)	μ_0 (mag arcsec ⁻²) (9)	h ($''$) (10)	q_d (11)	PA_d ($^\circ$) (12)	B/T (13)	$m_{i,bulge}$ (mag) (14)
NGC 4486B	yes	$r^{1/n}$	17.91 ± 0.40	2.73 ± 1.37	3.58 ± 0.35	0.85 ± 0.01	4.90 ± 0.01	1.00	12.58 ± 0.24
Galaxies from Sample B													
Abell 1836	yes	$r^{1/n}+exp.$	21.01 ± 0.36	9.49 ± 2.51	2.73 ± 0.33	0.89 ± 0.01	79.32 ± 19.50	21.92 ± 0.44	27.88 ± 12.46	0.60 ± 0.06	68.58 ± 0.73	0.54 ± 0.22	13.06 ± 0.29
NGC 821	yes	$r^{1/n}$	23.15 ± 0.08	111.25 ± 3.87	7.70 ± 0.15	0.59 ± 0.01	6.97 ± 0.01	1.00	9.75 ± 0.03
NGC 1068	yes	$r^{1/n}+exp.$	17.14 ± 0.09	10.27 ± 0.69	1.27 ± 0.04	0.65 ± 0.01	140.97 ± 5.52	18.30 ± 0.10	29.35 ± 1.26	0.99 ± 0.01	180.00 ± 0.11	0.33 ± 0.01	9.74 ± 0.09
NGC 2778	no	embedded disc
NGC 3031	yes	$r^{1/n}+exp.$	18.75 ± 0.02	50.02 ± 0.49	2.57 ± 0.02	0.72 ± 0.01	91.24 ± 0.60	18.79 ± 0.01	150.21 ± 0.60	0.50 ± 0.01	95.77 ± 0.02	0.33 ± 0.01	7.45 ± 0.01
NGC 3227	no	bar
NGC 3245	yes	$r^{1/n}+exp.$	17.45 ± 0.11	4.00 ± 0.35	1.60 ± 0.09	0.75 ± 0.01	100.76 ± 8.75	18.59 ± 0.18	20.66 ± 4.08	0.50 ± 0.02	101.64 ± 0.29	0.27 ± 0.04	11.83 ± 0.08
NGC 3377	yes	$r^{1/n}$	20.41 ± 0.07	43.52 ± 1.51	3.47 ± 0.07	0.70 ± 0.01	137.05 ± 0.02	1.00	9.63 ± 0.03
NGC 3379	no	bad
NGC 3384	yes	$r^{1/n}+exp.$	17.68 ± 0.09	8.31 ± 0.56	2.33 ± 0.08	0.84 ± 0.01	144.36 ± 5.65	19.57 ± 0.11	53.79 ± 2.32	0.47 ± 0.01	148.30 ± 0.09	0.40 ± 0.02	10.17 ± 0.09
NGC 3607	yes	$r^{1/n}$	21.14 ± 0.01	56.34 ± 0.22	4.70 ± 0.01	0.80 ± 0.01	38.34 ± 0.01	1.00	9.16 ± 0.01
NGC 3608	yes	$r^{1/n}$	24.20 ± 0.01	182.19 ± 0.72	9.03 ± 0.03	0.79 ± 0.01	175.16 ± 0.02	1.00	9.33 ± 0.01
NGC 3998	yes	$r^{1/n}+exp.$	17.47 ± 0.13	5.65 ± 0.73	2.29 ± 0.11	0.84 ± 0.01	45.48 ± 4.74	19.33 ± 0.29	25.51 ± 6.67	0.78 ± 0.03	54.96 ± 0.13	0.45 ± 0.05	10.80 ± 0.14
NGC 4026	no	bad
NGC 4258	no	bad
NGC 4261	yes	$r^{1/n}$	21.06 ± 0.01	48.82 ± 0.19	4.31 ± 0.01	0.77 ± 0.01	67.96 ± 0.01	1.00	9.47 ± 0.01
NGC 4342	no	embedded disc
NGC 4374	yes	$r^{1/n}$	20.63 ± 0.01	63.61 ± 0.06	4.10 ± 0.01	0.86 ± 0.01	37.32 ± 0.01	1.00	8.38 ± 0.01
NGC 4459	yes	$r^{1/n}$	23.23 ± 0.01	155.21 ± 0.61	7.44 ± 0.02	0.82 ± 0.01	13.91 ± 0.01	1.00	8.78 ± 0.01
NGC 4473	yes	$r^{1/n}+exp.$	18.05 ± 0.09	10.60 ± 0.71	2.23 ± 0.07	0.57 ± 0.01	3.26 ± 0.13	19.64 ± 0.11	38.14 ± 1.64	0.56 ± 0.01	1.46 ± 0.01	0.48 ± 0.02	10.44 ± 0.09
NGC 4486	no	light excess
NGC 4486A	no	bad
NGC 4564	no	embedded disc
NGC 4596	yes	$r^{1/n}+exp.$	21.49 ± 0.11	44.91 ± 3.01	4.43 ± 0.15	0.87 ± 0.01	14.90 ± 0.58	19.48 ± 0.11	32.71 ± 1.41	0.67 ± 0.01	162.85 ± 0.10	0.78 ± 0.04	9.94 ± 0.09
NGC 4649	yes	$r^{1/n}+exp.$	18.18 ± 0.09	14.88 ± 1.00	1.63 ± 0.05	0.85 ± 0.01	7.98 ± 0.31	19.03 ± 0.11	54.15 ± 2.33	0.78 ± 0.01	13.78 ± 0.01	0.30 ± 0.01	9.56 ± 0.08
NGC 4697	yes	$r^{1/n}$	21.82 ± 0.01	128.68 ± 0.12	4.96 ± 0.01	0.69 ± 0.01	63.86 ± 0.01	1.00	8.34 ± 0.01
NGC 5576	yes	$r^{1/n}$	22.42 ± 0.07	77.58 ± 2.70	8.71 ± 0.17	0.69 ± 0.01	177.21 ± 0.02	1.00	9.62 ± 0.03
NGC 5845	yes	$r^{1/n}$	17.63 ± 0.27	4.06 ± 0.72	3.45 ± 0.26	0.66 ± 0.01	50.79 ± 0.04	1.00	11.78 ± 0.18

NOTES. — Col.(1): Galaxy name. Col.(2): Result of the two dimensional decomposition of the galaxy surface brightness distribution: yes = successful fit; no = unsuccessful fit; Col.(3): Comments about the fit: $r^{1/n}$ = the galaxy has been successfully fitted with a Sérsic law; $r^{1/n}+exp.$ = the galaxy has been successfully fitted with a Sérsic bulge and exponential disc; bad = inadequate one or two-component fit; Freeman II disc = the disc seems to follow a Freeman Type II law; embedded disc = the bulge and disc components have been fitted with a Sérsic and exponential law, respectively. But, the bulge is dominating the light contribution at both small and large radii; bar = a strong bar is present in addition to the bulge and disc components; light excess = the light excess measured at large radii can not be parametrised with an exponential function. A cut-off profile (e.g., Oemler 1976) is required.

Col.(4): Effective surface brightness of the bulge. Col.(5): Effective radius of the bulge. Col.(6): Shape parameter of the bulge. Col.(7): Axial ratio of the bulge isophotes. Col.(8): Position angle of the bulge major-axis. Col.(9): Central surface brightness of the disc. Col.(10): Scale length of the disc. Col.(11): Axial ratio of the disc isophotes. Col.(12): Position angle of the disc major-axis. Col.(13): Bulge-to-total luminosity ratio. Col.(14): Total magnitude of the bulge.

Table 5. Fitting parameters and correlation coefficients for the different relations

x	Sample	N	ρ	P	α	β	ϵ	ϵ_{int}	x_0
σ_e	B	49	0.85	< 0.1%	8.19 ± 0.07	4.17 ± 0.32	0.41 ± 0.06	0.36 ± 0.07	200 km s^{-1}
	A+B	143	0.69	< 0.1%	7.99 ± 0.06	4.42 ± 0.30	0.44 ± 0.05	...	
	comparison	30	0.64	< 0.1%	7.88 ± 0.20	4.97 ± 1.22	0.52 ± 0.10	...	
$L_{i,\text{bulge}}$	B	19	0.26	26%	8.60 ± 0.30	0.47 ± 0.31	0.56 ± 0.10	0.58 ± 0.11	$10^{11} M_\odot$
	A+B	57	0.34	1%	8.17 ± 0.22	0.79 ± 0.24	0.81 ± 0.13	...	
	comparison	30	0.22	24%	7.24 ± 0.65	0.45 ± 0.53	0.85 ± 0.32	...	
M_{bulge}	B	19	0.46	4.6%	8.25 ± 0.13	0.79 ± 0.26	0.47 ± 0.06	0.46 ± 0.07	$10^{11} M_\odot$
	A+B	57	0.52	< 0.1%	7.84 ± 0.12	0.91 ± 0.16	0.61 ± 0.08	...	
	comparison	30	0.44	1.8%	7.79 ± 0.39	1.23 ± 0.53	0.77 ± 0.20	...	
n	B	19	-0.1	38%	8.25 ± 0.18	0.06 ± 0.80	0.60 ± 0.12	0.61 ± 0.13	3
	A+B	57	0.24	7.6%	7.39 ± 0.19	1.25 ± 0.60	0.93 ± 0.17	...	
	comparison	30	0.30	11%	6.96 ± 0.36	1.84 ± 0.89	0.97 ± 0.28	...	
$\langle \mu_{e,\text{bulge}} \rangle$	B	19	-0.0	46%	8.21 ± 0.19	1.78 ± 3.40	0.60 ± 0.10	0.62 ± 0.12	$19 \text{ mag arcsec}^{-2}$
	A+B	57	0.16	23%	7.47 ± 0.20	4.91 ± 4.00	0.96 ± 0.16	...	
	comparison	30	0.11	53%	6.90 ± 0.44	7.31 ± 7.75	1.08 ± 0.35	...	
L_{gal}	B	28	0.44	2%	8.69 ± 0.22	1.14 ± 0.40	0.53 ± 0.10	0.52 ± 0.11	$10^{11} M_\odot$
	A+B	90	0.34	0.15%	7.92 ± 0.23	1.33 ± 0.35	0.91 ± 0.12	...	
	comparison	30	0.26	17%	7.41 ± 0.55	1.22 ± 0.99	1.06 ± 0.21	...	
$M_{\star,\text{gal}}$	B	28	0.51	0.59%	8.21 ± 0.10	1.43 ± 0.36	0.49 ± 0.09	0.42 ± 0.14	$10^{11} M_\odot$
	A+B	90	0.43	< 0.1%	7.47 ± 0.15	1.42 ± 0.28	0.81 ± 0.11	...	
	comparison	30	0.40	3%	7.17 ± 0.31	1.55 ± 0.75	0.88 ± 0.14	...	
V_c	B	23	0.72	< 0.1%	7.82 ± 0.15	3.29 ± 0.61	0.54 ± 0.08	0.51 ± 0.09	200 km s^{-1}
	A+B	88	0.38	< 0.1%	6.91 ± 0.16	4.02 ± 0.87	0.84 ± 0.11	...	
	comparison	30	0.37	4.5%	6.82 ± 0.31	3.59 ± 1.57	0.84 ± 0.19	...	
$M_{e,\text{gal}}$	B	24	0.55	0.3%	8.17 ± 0.13	0.83 ± 0.27	0.54 ± 0.11	0.53 ± 0.12	$10^{11} M_\odot$
	A+B	51	0.49	< 0.1%	7.86 ± 0.09	1.00 ± 0.17	0.49 ± 0.07	...	
$M_{\text{dyn,gal}}$	B	6	0.24	35%	7.62 ± 0.19	0.32 ± 0.87	0.46 ± 0.16	0.53 ± 0.02	$10^{11} M_\odot$
	A+B	47	0.13	36%	6.10 ± 0.39	0.55 ± 0.59	0.96 ± 0.31	...	

NOTES. — For the variable x a correlation of the form $\log(M_\bullet/M_\odot) = \alpha + \beta \log(x/x_0)$ is assumed for the N data points. For Samples A+B and the comparison sample, the total scatter ϵ is defined as the root-mean square deviation in $\log(M_\bullet/M_\odot)$ from the fitted relation assuming no measurement errors. For sample B, the total scatter takes measurement errors in both variables into account.

Table 6. Fitting parameters and correlation coefficients for the different linear combinations

x	y	Sample	N	ρ	P	γ	α	β	ϵ	ϵ_{int}	x_0	y_0
σ_e	$r_{e,\text{bulge}}$	B	19	0.81	< 0.1%	8.34 ± 0.13	3.93 ± 0.68	0.32 ± 0.21	0.37 ± 0.06	0.36 ± 0.07	200 km s^{-1}	5 kpc
		A+B	57	0.70	< 0.1%	8.13 ± 0.11	4.37 ± 0.56	0.27 ± 0.14	0.39 ± 0.04	...		
		comparison	30	0.68	< 0.1%	5.77 ± 2.69	4.95 ± 1.98	0.90 ± 0.53	0.37 ± 0.09	...		
$L_{i,\text{bulge}}$	$r_{e,\text{bulge}}$	B	19	0.11	66%	8.62 ± 0.30	0.41 ± 0.40	0.19 ± 0.44	0.60 ± 0.10	0.63 ± 0.11	$10^{11} L_{\odot}$	5 kpc
		A+B	57	0.33	1.2%	8.16 ± 0.25	0.72 ± 0.57	0.01 ± 0.60	0.81 ± 0.13	...		
		comparison	30	0.20	28%	5.18 ± 4.23	0.07 ± 0.70	0.71 ± 1.14	0.88 ± 0.26	...		
σ_e	$L_{i,\text{bulge}}$	B	19	0.79	< 0.1%	8.33 ± 0.19	3.88 ± 0.70	0.15 ± 0.20	0.39 ± 0.06	0.38 ± 0.07	200 km s^{-1}	$10^{11} L_{\odot}$
		A+B	57	0.68	< 0.1%	8.11 ± 0.17	4.42 ± 0.63	0.14 ± 0.18	0.41 ± 0.05	...		
		comparison	30	0.63	< 0.1%	7.83 ± 0.54	4.97 ± 2.48	-0.05 ± 0.30	0.52 ± 0.10	...		
M_{bulge}	$r_{e,\text{bulge}}$	B	19	0.80	< 0.1%	7.54 ± 0.15	2.08 ± 0.34	-1.82 ± 0.33	0.37 ± 0.06	0.29 ± 0.08	$10^{11} M_{\odot}$	5 kpc
		A+B	57	0.70	< 0.1%	7.33 ± 0.16	2.19 ± 0.28	-1.92 ± 0.33	0.39 ± 0.04	...		
		comparison	30	0.49	0.9%	11.92 ± 1.92	2.07 ± 0.91	-1.46 ± 0.83	0.62 ± 0.13	...		
σ_e	M_{bulge}	B	19	0.81	< 0.1%	8.22 ± 0.10	3.29 ± 0.61	0.32 ± 0.22	0.37 ± 0.06	0.36 ± 0.07	200 km s^{-1}	$10^{11} M_{\odot}$
		A+B	57	0.70	< 0.1%	8.03 ± 0.09	3.83 ± 0.65	0.27 ± 0.14	0.39 ± 0.04	...		
		comparison	30	0.66	< 0.1%	8.08 ± 0.28	4.09 ± 1.84	0.46 ± 0.44	0.45 ± 0.10	...		
σ_e	$r_{e,\text{gal}}$	B	28	0.83	< 0.1%	8.27 ± 0.10	4.03 ± 0.47	0.24 ± 0.23	0.36 ± 0.05	0.34 ± 0.06	200 km s^{-1}	5 kpc
		A+B	90	0.71	< 0.1%	8.02 ± 0.09	4.81 ± 0.40	0.03 ± 0.21	0.40 ± 0.04	...		
		comparison	30	0.64	< 0.1%	7.90 ± 0.32	4.99 ± 1.97	0.09 ± 0.72	0.52 ± 0.10	...		
$L_{i,\text{gal}}$	$r_{e,\text{gal}}$	B	28	0.53	0.4%	8.74 ± 0.29	1.59 ± 0.76	-0.72 ± 0.74	0.56 ± 0.12	0.57 ± 0.14	$10^{11} L_{\odot}$	5 kpc
		A+B	90	0.57	< 0.1%	8.45 ± 0.25	3.15 ± 0.57	-2.76 ± 0.64	0.77 ± 0.10	...		
		comparison	30	0.58	0.2%	7.73 ± 0.75	3.06 ± 1.79	-3.69 ± 2.03	0.97 ± 0.20	...		
σ_e	$L_{i,\text{gal}}$	B	28	0.84	< 0.1%	8.27 ± 0.20	4.02 ± 0.81	0.12 ± 0.37	0.37 ± 0.05	0.35 ± 0.0	200 km s^{-1}	$10^{11} L_{\odot}$
		A+B	90	0.70	< 0.1%	8.04 ± 0.13	4.74 ± 0.51	0.05 ± 0.23	0.41 ± 0.04	...		
		comparison	30	0.64	< 0.1%	7.90 ± 0.36	4.95 ± 1.99	0.06 ± 0.52	0.52 ± 0.11	...		
$M_{\star,\text{gal}}$	$r_{e,\text{gal}}$	B	28	0.62	< 0.1%	7.53 ± 0.27	3.85 ± 0.84	-3.19 ± 1.03	0.68 ± 0.16	0.58 ± 0.15	$10^{11} M_{\odot}$	5 kpc
		A+B	90	0.59	< 0.1%	7.29 ± 0.15	2.74 ± 0.41	-2.33 ± 0.51	0.66 ± 0.09	...		
		comparison	30	0.63	< 0.1%	6.74 ± 0.51	3.07 ± 1.65	-3.51 ± 1.82	0.78 ± 0.19	...		
σ_e	$M_{\star,\text{gal}}$	B	28	0.83	< 0.1%	8.21 ± 0.08	3.59 ± 1.23	0.32 ± 0.55	0.37 ± 0.05	0.34 ± 0.05	200 km s^{-1}	$10^{11} M_{\odot}$
		A+B	90	0.70	< 0.1%	8.02 ± 0.07	4.68 ± 0.56	0.08 ± 0.24	0.41 ± 0.58	...		
		comparison	30	0.68	< 0.1%	7.93 ± 0.21	4.28 ± 1.79	0.61 ± 0.54	0.48 ± 0.11	...		

NOTES. — For the variable (x, y) a correlation of the form $\log(M_{\bullet}/M_{\odot}) = \gamma + \alpha \log(x/x_0) + \beta \log(y/y_0)$ is assumed for the N data points. For Samples A+B and the comparison sample, the total scatter ϵ is defined as the root-mean square deviation in $\log(M_{\bullet}/M_{\odot})$ from the fitted relation assuming zero measurement errors. For sample B, the total scatter takes measurement errors for all the variables into account.

This paper has been typeset from a \TeX / \LaTeX file prepared by the author.